Supporting Information for

Integrated Polyanion-Layered Oxide Cathodes Enabling 100,000 Cycle Life for Sodium-Ion Batteries

Zhiyu Zou,[1,2,4] Yongbiao Mu,[1,2,4] Meisheng Han,*[1,2] Youqi Chu,[1,2] Jie Liu,[1,2] Kunxiong Zheng,[1,2] Qing Zhang,[1,2] Manrong Song,[1,2] Qinping Jian,[3] Yilin Wang,[1,2] Hengyuan Hu,[1,2] Fenghua Yu,[1,2] Wenjia Li,[1,2] Lei Wei,[1,2] Lin Zeng,*[1,2] and Tianshou Zhao*[1,2]

[1]Shenzhen Key Laboratory of Advanced Energy Storage, Department of Mechanical and Energy Engineering, Southern University of Science and Technology, Shenzhen 518055, China

[2]SUSTech Energy Institute for Carbon Neutrality, Southern University of Science and Technology, Shenzhen 518055, China

[3]Department of Mechanical and Aerospace Engineering, The Hong Kong University of Science and Technology, Clear Water Bay, Kowloon, Hong Kong SAR, China

[4]These authors contributed equally: Zhiyu Zou, Yongbiao Mu.

*Corresponding Authors. E-mail address: hanms@sustech.edu.cn (M. Han); zengl3@sustech.edu.cn (L. Zeng); zhaots@sustech.edu.cn (T. Zhao)

Experimental Section:

The $Na_{3.5}Fe_{0.5}V_{1.5}(PO_4)_3$-$V_2O_3$ composition (designated as NFVP-VO) were prepared via a ball mill assisted sol−gel method. In detail, vanadium (3^+) acetylacetonate (Macklin, AR), ferrous (2^+) acetylacetonate (Macklin, AR), CH_3COONa (5% excess, Macklin, AR), and H_3PO_4 (Macklin, ≥ 85 wt.% in H_2O) were added into the citric acid solution (ethanol: deionized water = volume ratio 1: 1, citric acid: metal element = molar ratio 1.5: 1) according to the stoichiometric ratio under magnetic stirring. Citric acids were used as both carbon sources and chelating agent. Then the mixture was heated in a water bath at 80 °C under magnetic stirring to evaporate the solvent to obtain a gel. The gel was further dried at 110 °C for 12 h and then transferred to a high-energy ball mill with stainless-steel milling balls (weight ratio of 1:3), which were milled for 2h to get the precursor powder. Subsequently, the precursor was subjected to different calcination temperatures (650~750°C) to optimize the annealing treatment condition. Indeed, the obtained target sample was sintered at 700 °C for 8 h in argon atmosphere (at a heating rate of 2 °C min^{-1}). As a control, $Na_{3.5}Fe_{0.5}V_{1.5}(PO_4)_3$ (designated as NVFP) was synthesised via the same process with vanadium source change from vanadium (3^+) acetylacetonate to ammonium vanadate (5^+). The commercial $Na_3V_2(PO_4)_3$ (MA-EN-CA-0044, designated as NVP) and commercial V_2O_3 (CAS:1314-34-7) was bought from Canrud and Aladdin, respectively, for comparison.

Material characterization:

The morphologies of all samples were characterized by Hitachi SU-8230 field emission scanning electron microscopy (SEM, Hitachi SU-8230). Transmission Electron Microscope (TEM), energy-dispersive X-ray analysis (EDX), and elemental mapping were performed using a Talos

instrument with an acceleration voltage of 300 kV. X-ray photoelectron spectra (XPS, Escalab 250Xi) were acquired on a Thermo SCIENTIFIC ESCALAB 250Xi with Al Kα (hu = 1486.8 eV) as the excitation source. Before XPS tests, the cycled electrode was washed with PC three times to remove residual electrolytes and then dried by evaporation in a vacuum chamber. The electrode was pasted on the loading chamber with a vacuum transfer function. In the process of transfer, the sample was sealed in the loading chamber and always protected by Ar atmosphere. The electrode was not exposed to any reactive atmosphere during the whole process. Raman spectra were performed on a HORIBA LabRAM HR Evolution using a 532 nm laser as the excitation source. The acquisition time was 15 s with two accumulations during Raman spectrum collection. Thermal Gravity Analysis (TGA) were performed in oxygen using the Netzsch TG 209 F3 over the temperature range of room temperature to 800 °C with a heating rate of 10 °C min^{-1}. Raman spectra were performed on a HORIBA LabRAM HR Evolution using a 532 nm laser as the excitation source. Brunauer-Emmett-Teller (BET) surface areas were calculated from nitrogen sorption isotherms obtained at 77 K on an BELSORP MINI X instrument. Inductively coupled plasma-optical emission spectroscopy (ICP-OES) were used to analysis the elemental ratio of the as-prepared samples using Agilent 720ES. (Instrument parameters: RF Power: 1.20 KW, Plsama flow: 15.0 L/min, Auxiliary flow:1.50 L/min, Nebulizer flow：0.75 L/min, Sample uptake delay:15 s, Instrument stabilization delay：15 s, Replicate read time：2 s, Replicates: 3 times). Powder resistivity and compaction density was test by IEST, PRCD2100 to evaluate the powder properties of all materials. For X-ray absorption near-edge structure (XANES) measurement, electrode samples were prepared by disassembling coin cells that were charged/discharged to a specific voltage, and then rinsed with propylene carbonate for 2 min. For Ultraviolet Photoelectron Spectroscopy (UPS)

measurement, the Valance band (VB) spectra were measured with a monochromatic He I light source (21.2eV) in Thermo Scientific Nexsa. A sample bias of -5 V was applied to observe the secondary electron cutoff (SEC). The work function can be determined by the difference between the photon energy and the binding energy of the secondary cutoff edge.

Electrochemical measurements:

To assess the electrochemical behavior of all samples, CR2032-type coin cells were assembled. The working electrodes are composed of active materials, conductive additive (Super P), and binder (PVDF, Solef 5130, Solvay) at a mass ratio of 8:1:1. These materials are fully milled and a N-methylpyrrolidone (NMP, Tci) solution containing 2 wt% PVDF is added and then mixed with micro-vibrating ball mill (MSK-SFM-12M) for 10 min to make them a slurry and then coated on aluminum foil to prepare the working electrode. The obtained electrodes are predried in a drying/heating chamber with forced convection at 60 °C for 2 h and thoroughly dried under vacuum at 80 °C for at least 12 h. While sodium metal piece is served as the counter/reference electrode, and Whatman GF-D glass fiber is used as separator. The electrolyte is 1M $NaClO_4$ in propylene carbonate (PC) with 5 vol% fluoroethylene-carbonate (FEC). The mass loading of active materials is around 2.00 mg cm^{-2}, while the resolution of the balance is 0.01 mg. The amount of electrolyte in each coin cell is around 150 μl. The electrochemical performance was evaluated using a Neware battery test system (Shenzhen, China) at room temperature. Specially, the nominal capacity of 1 C is designated as 100 mAh g^{-1} and no rest time is set between charging and discharging when a long cycle test is performed. The Na-ion pouch cells were assembled with kg-level NVFP-VO as the cathode and the commercial hard carbon (HC, Kuraray Co. type 2, Japan) as anode, Celgard 2325 membrane as the separator, 1M $NaClO_4$ in PC with 5 vol% FEC as electrolyte (same as coin-type cells) and Al-plastic film as packaging. The

composition of the cathode slurry is made of 95 wt% active materials, 2 wt% Super P, 2 wt% PVDF, and 1 wt% carbon nano tube (CNT). The composition of the HC slurry is made of 95 wt% active materials, 2 wt% Super P, 1 wt% carboxymethyl cellulose (CMC) and 2 wt% styrene butadiene rubber (SBR). The effective mass surface density ratio of cathode to anode was about 1.2:1 with reference to the corresponding reversible capacities. The prepared cathode and anode electrodes are trimmed to a dimension of 130 × 50 mm for pouch cell assembly, with the cathode and anode alternately stacked in a dry room and the final pre-sealing of the completed pouch cell, following the filling of the electrolyte, was carried out inside a glove box (H_2O and O_2 concentration less than 0.01 ppm). The details and parameters of the pouch cell are summaried in **Table S4**. Cyclic voltammograms (CVs) profiles at various scan rates from 0.1 to 2 mV s^{-1} and Electrochemical impedance spectra (EIS) measurements were conducted using a Bio-Logic EC-LAB VMP-300 electrochemical workstation with a frequency range of 100 kHz to 10 mHz. For the galvanostatical current intermittent titration technology (GITT) measurements, all the electrodes are galvanostatically charged or discharged with 20 mA g^{-1} current pulse for 10 min, followed by a 40 min relaxation step to obtain a nearly steady state.

DFT computational methods:

All the DFT calculations were conducted based on the Vienna Ab-inito Simulation Package (VASP).[1,2] The exchange-correlation effects were described by the Perdew-Burke-Ernzerhof (PBE) functional within the generalized gradient approximation (GGA) method.[3] The projected augmented wave (PAW) potentials[4,5] were chosen to describe the ionic cores and take valence electrons into account using a plane wave basis set with a kinetic energy cutoff of 520 eV. Partial occupancies of the Kohn−Sham orbitals were allowed using the Gaussian smearing method with a width of 0.05 eV. The electronic energy was considered self-consistent when the energy change was

smaller than 10^{-5} eV. A geometry optimization was considered convergent when the energy change was smaller than 0.03 eV $Å^{-1}$. During structural optimizations, a 3×2×2 k-point grid in the Brillouin zone was used for k-point sampling, and all atoms were allowed to relax. In our structure, the U correction is used for Fe (4.81 eV) atoms. Na ion pathway can be calculated using the nudged elastic band (NEB) method with the transition state of an elementary reaction step. In the NEB method, the path between the reactant(s) and product(s) was discretized into a series structural image. The intermediate images were relaxed until the perpendicular forces were smaller than 0.05 eV/Å.

Single particle COMSOL computational models:

Concentration model

This model was defined by the law of mass conservation and electroneutrality assumption of related ions without considering the possible side reactions. Create the rectangle domain with 3×2.5×2.5um as the model area. The vertical boundary was assumed to be insulating. The middle region is the area where the electrolyte and ions flow. In order to demonstrate the differences between the two materials, in the first model, we constructed a rectangular body and assigned material properties to NVP. In the second model, we built a rectangular body of the same size and constructed multiple spheres within it, where the rectangular body assigned material properties to NVFP/C and the spheres assigned material properties to V_2O_3.The initial Na^+ ion concentration in the electrolyte is set to 1000 mol m^{-3}.

Using the tertiary current distribution and concentration diffusion equation to track the current and concentration distribution, the flux of each ion in the electrolyte can be calculated by Nernst-Planck equation.

$$N_i = -D_i\left(\nabla c_i + \frac{F}{RT} z_i c_i \nabla \emptyset_l\right), \qquad i = 1,2,\dots,n$$

Where D_i, N_i, c_i, z_i, F, T R, and $\emptyset_l$ denote the diffusion coefficient, the flux, the concentration, the charge number, the Faradaic constant, temperature, gas

constant, and electrolyte potential, respectively. l stands for the position along the diffusion region of thickness d ($0 < l < d$). Based on the steady-state continuity equations and the law of mass conservation, we have

$$\frac{\partial c_i}{\partial t} + \nabla \cdot N_i = 0$$

and the electroneutrality assumption was represented as

$$F \sum_{i=1}^{n} z_i c_i = 0$$

The boundary condition was set as followed:

$$\vec{n} \cdot \mathrm{J} = 0$$

Mechanical equations

To focus on the essential physical effects of sodiation on stress generation, a simple elastic model is adopted to evaluate the deformation and stress states during Na insertion. The total strain rate $\dot{\varepsilon}_{ij}$ is taken to be the sum of two contributions

$$\dot{\varepsilon}_{ij} = \dot{\varepsilon}_{ij}^{c} + \dot{\varepsilon}_{ij}^{e} \quad (1)$$

Where $\dot{\varepsilon}_{ij}$ is the chemical strain rate caused by lithiation and is proportional to the rate of the normalized Na concentration c

$$\dot{\varepsilon}_{ij}^{c} = \beta_{ij}\dot{c} \quad (2)$$

where β_{ij} is the sodiation expansion coefficient, and c varies between 0 (pristine) and 1 (fully sodiated). In Eq. (1), denotes the elastic strain rate and obeys Hooke's law.

$$\dot{\varepsilon}_{ij}^{e} = \frac{1}{E}[(1+v)\dot{\sigma}_{ij} - v\dot{\sigma}_{kk}\delta_{ij}] \quad (3)$$

where E is Young's modulus, v is Poisson's ratio, $\dot{\sigma}_{ij} = 1$ when $i = j$ and $\delta_{ij} = 0$ otherwise, and repeated indices mean summation.

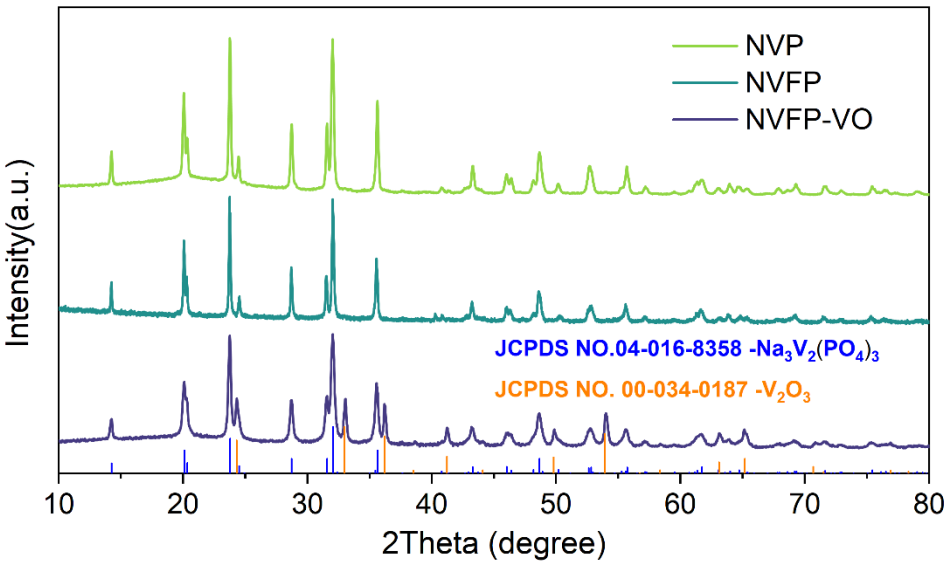

Figure S1. XRD results of NVP, NVFP, and NVFP-VO samples.

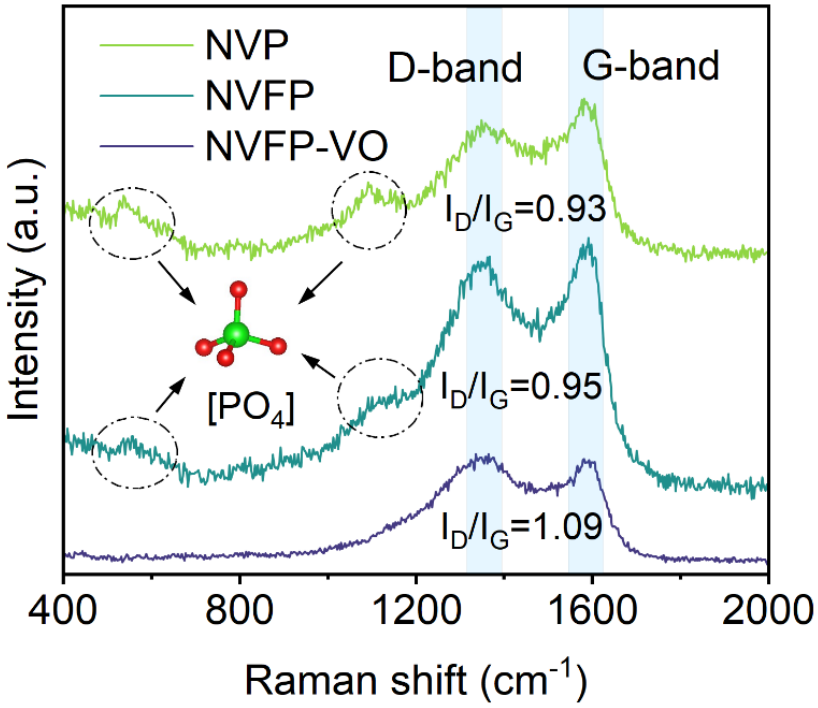

Figure S2. Raman spectra of NVP, NVFP, and NVFP-VO samples.

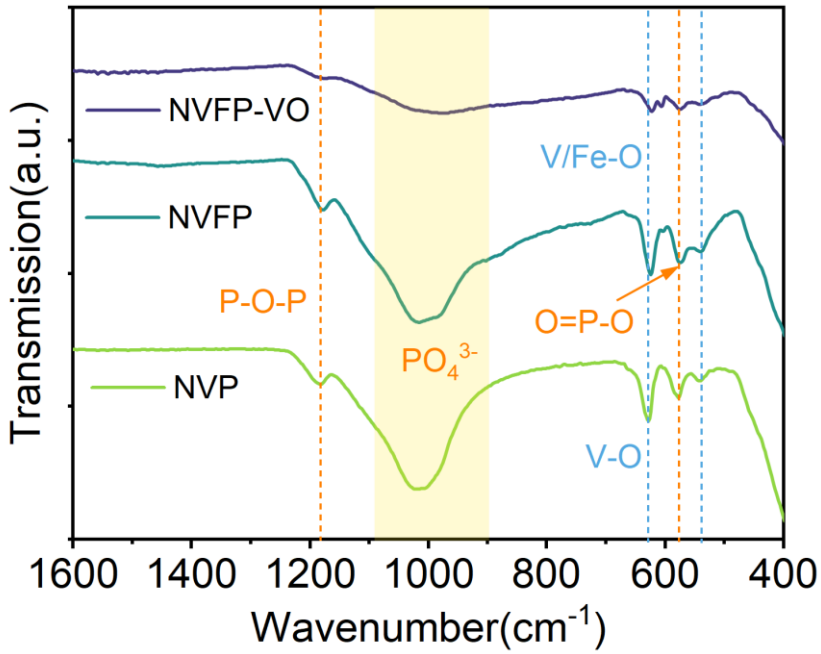

Figure S3. FTIR spectra of NVP, NVFP, and NVFP-VO samples.

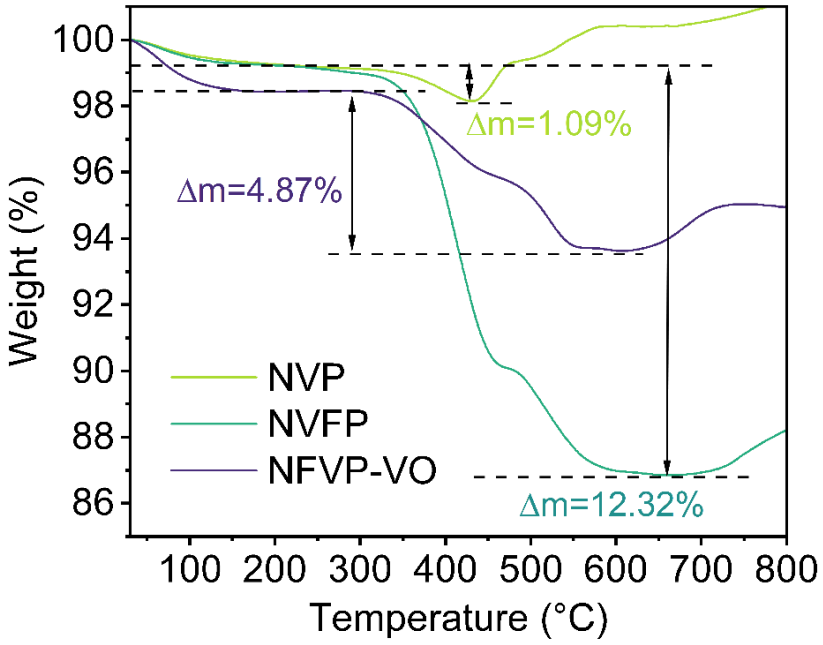

Figure S4. TGA curves of NVP, NVFP, and NVFP-VO samples.

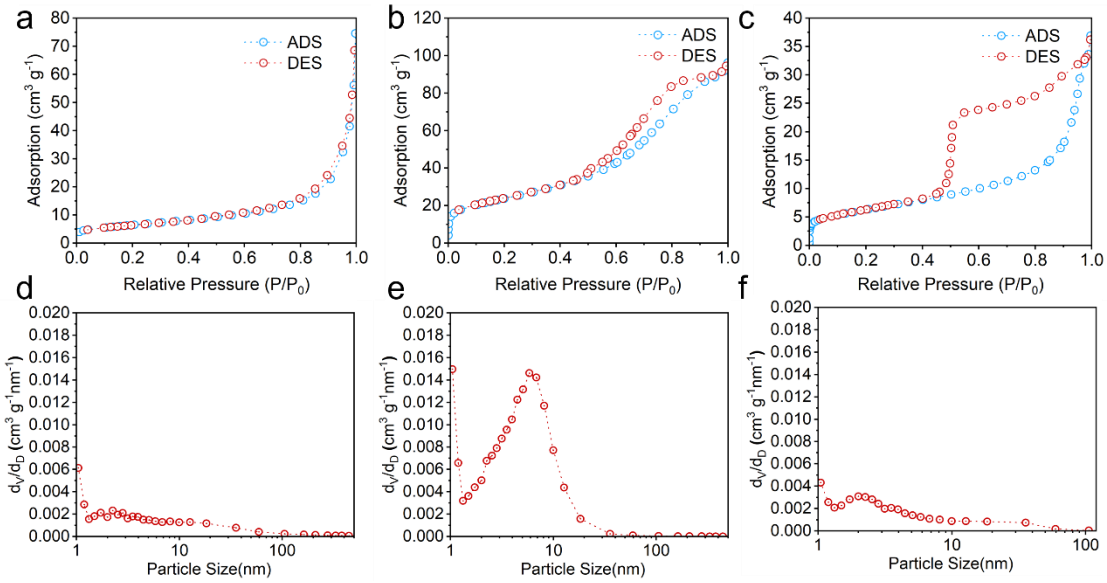

Figure S5. The surface area and pore size of **a, d** NVP, **b, e** NVFP, and **c, f** NVFP-VO samples, which shows the Brunauer–Emmett–Teller surface area of 22.849, 84.869, 22.452 m^2 g^{-1} and an average mesoporous distribution about 16.673, 5.883, 8.423 nm, respectively.

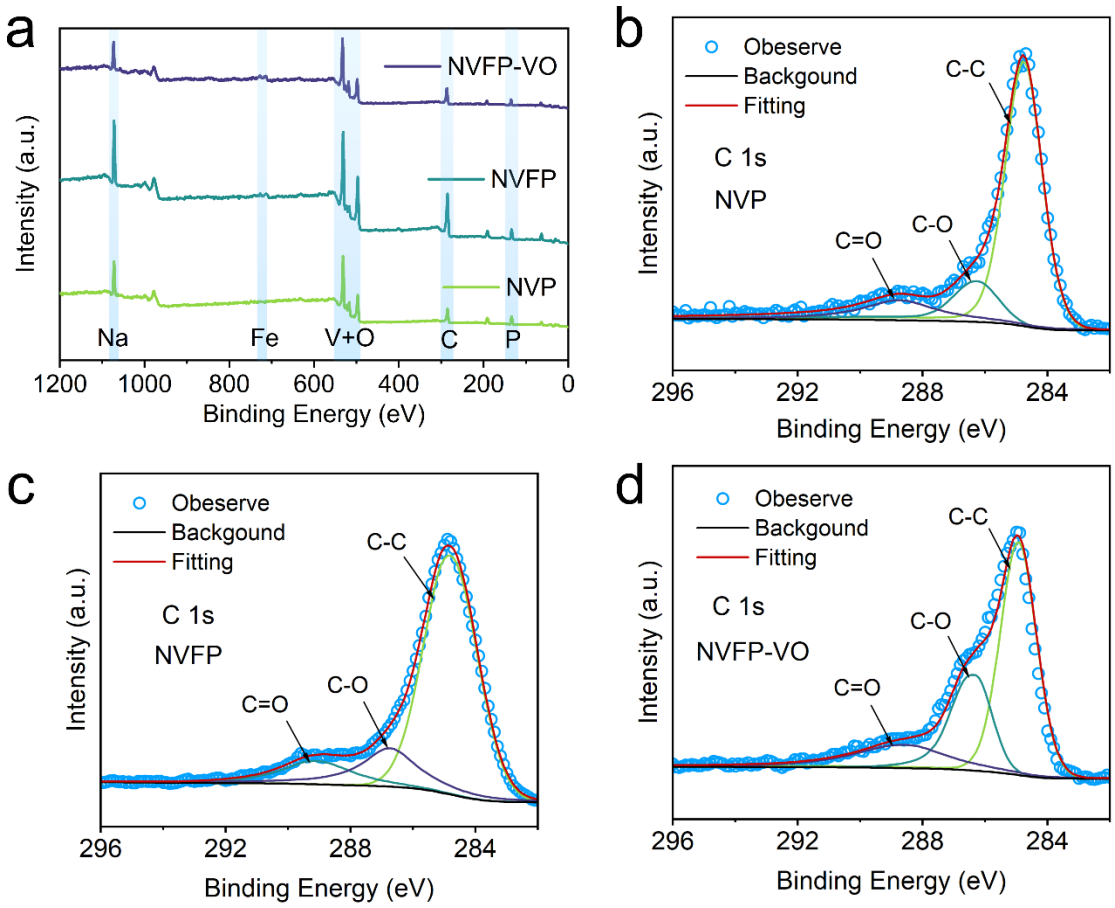

Figure S6. a XPS full spectra and high-resolution C1s spectra of **b** NVP, **c** NVFP, and **d** NVFP-VO samples.

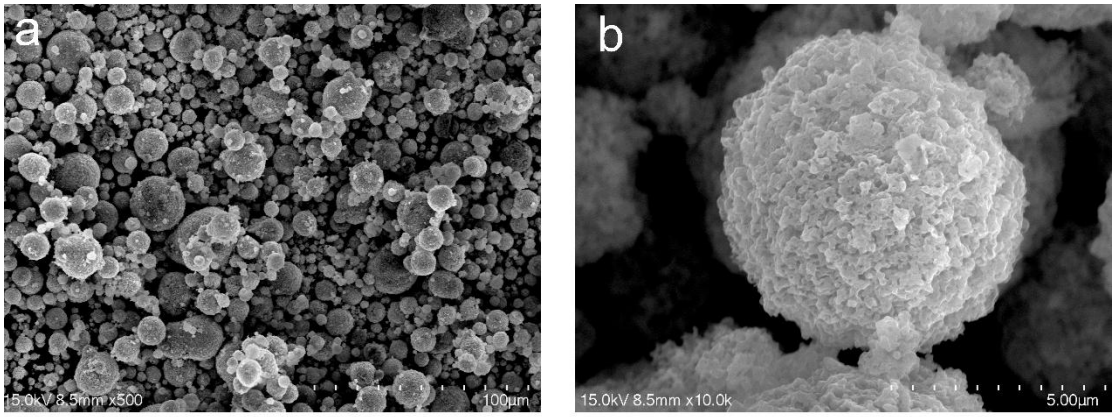

Figure S7. SEM images of **a** NVP, and **b** enlargement NVP sample.

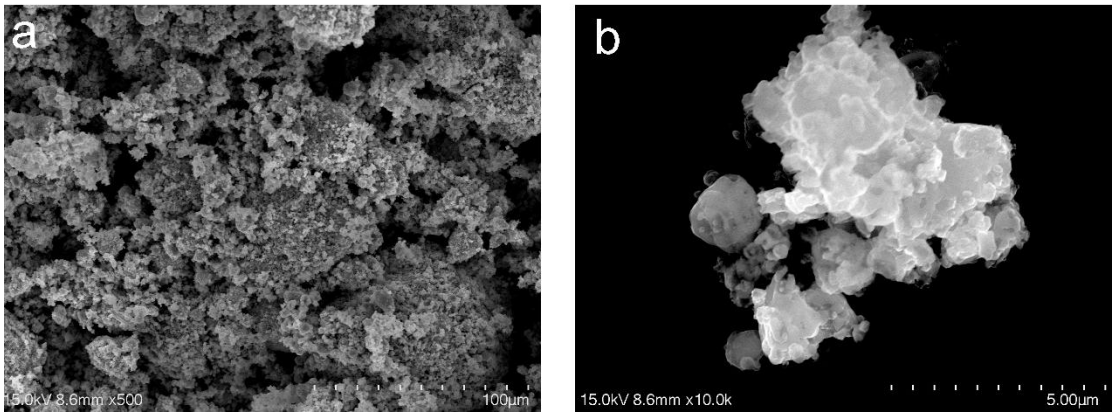

Figure S8. SEM images of **a** NVFP, and **b** enlargement NVFP sample.

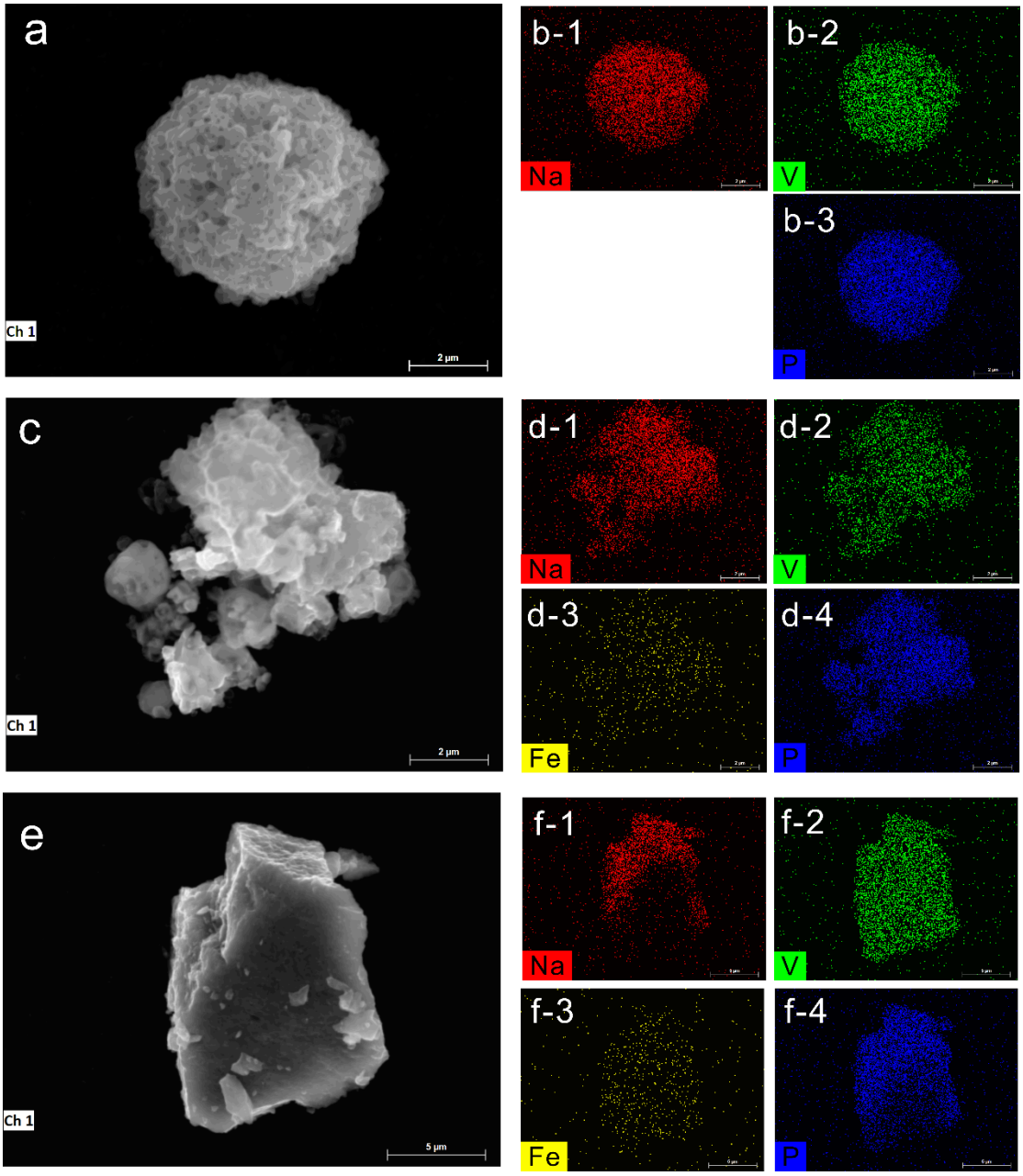

Figure S9. Single particle SEM images of **a** NVP, **c** NVFP, and **e** NVFP-VO samples and corresponding EDS of $\mathbf{b}_{1\text{-}3}$ NVP, $\mathbf{d}_{1\text{-}3}$ NVFP, and $\mathbf{f}_{1\text{-}3}$ NVFP-VO samples.

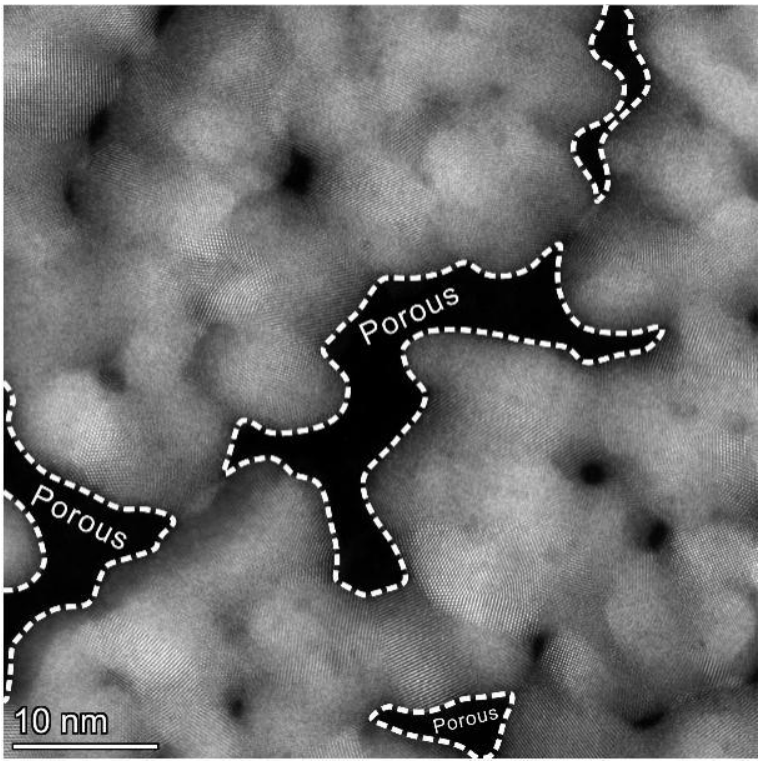

Figure S10. STEM images of porous matrix structure in NVFP-VO samples.

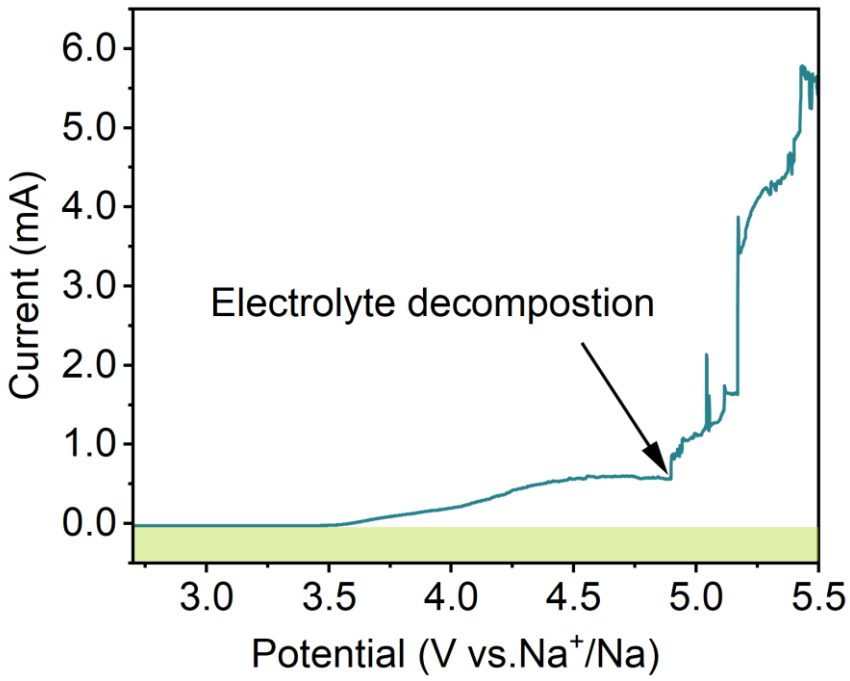

Figure S11. Linear sweep voltammetry curves at a scan rate of 1 mV s^{-1} of the electrolyte (1 M $NaClO_4$ in PC solution with 5 vol% FEC).

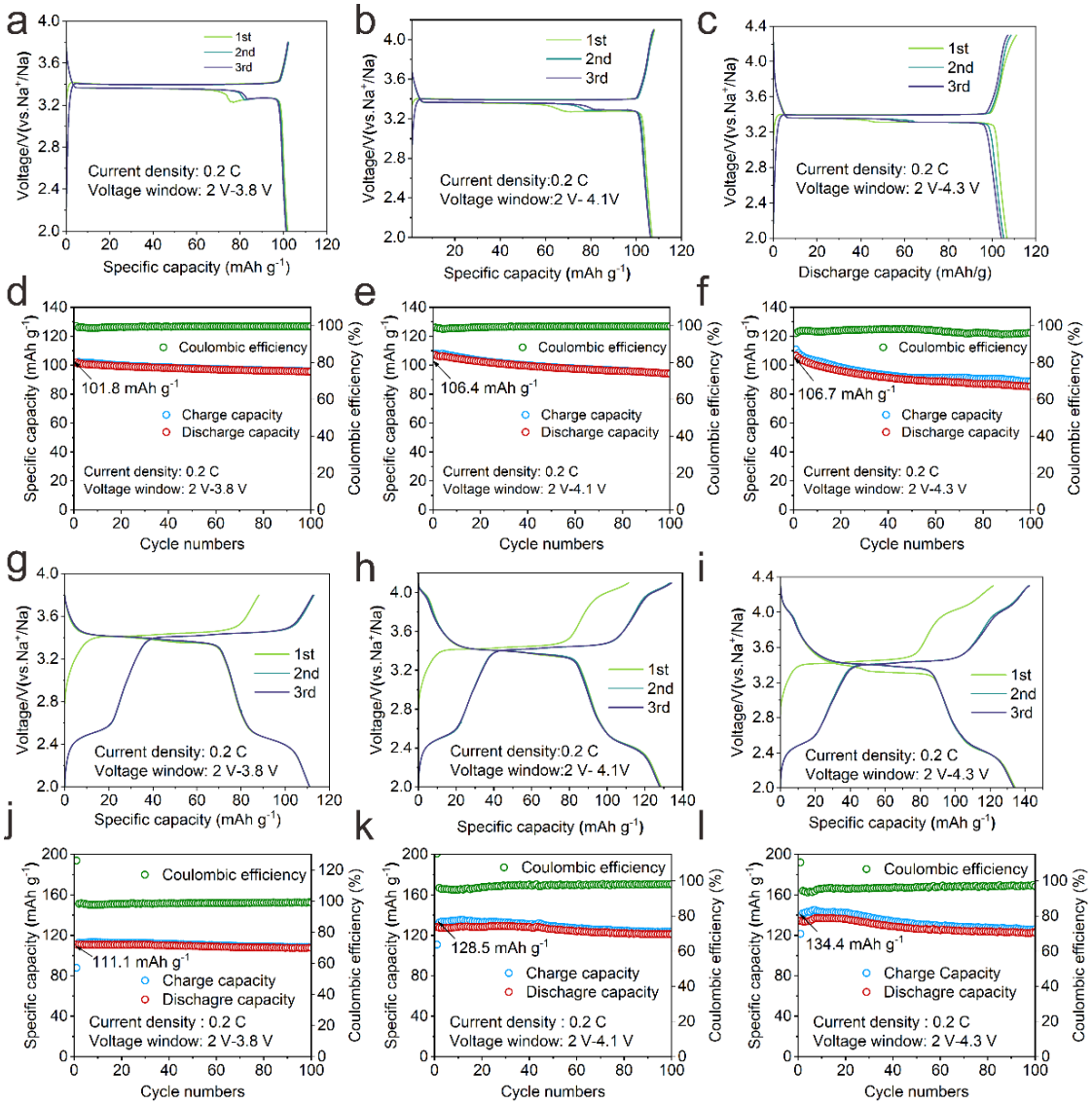

Figure S12. Charge-discharge curves of **a-c** NVP and **g-i** NVFP-VO; **d-f** the cyclability of NVP and **j-l** NVFP-VO at 0.2 C between 2-3.8V, 2-4.1V, 2-4.3V voltage windows.

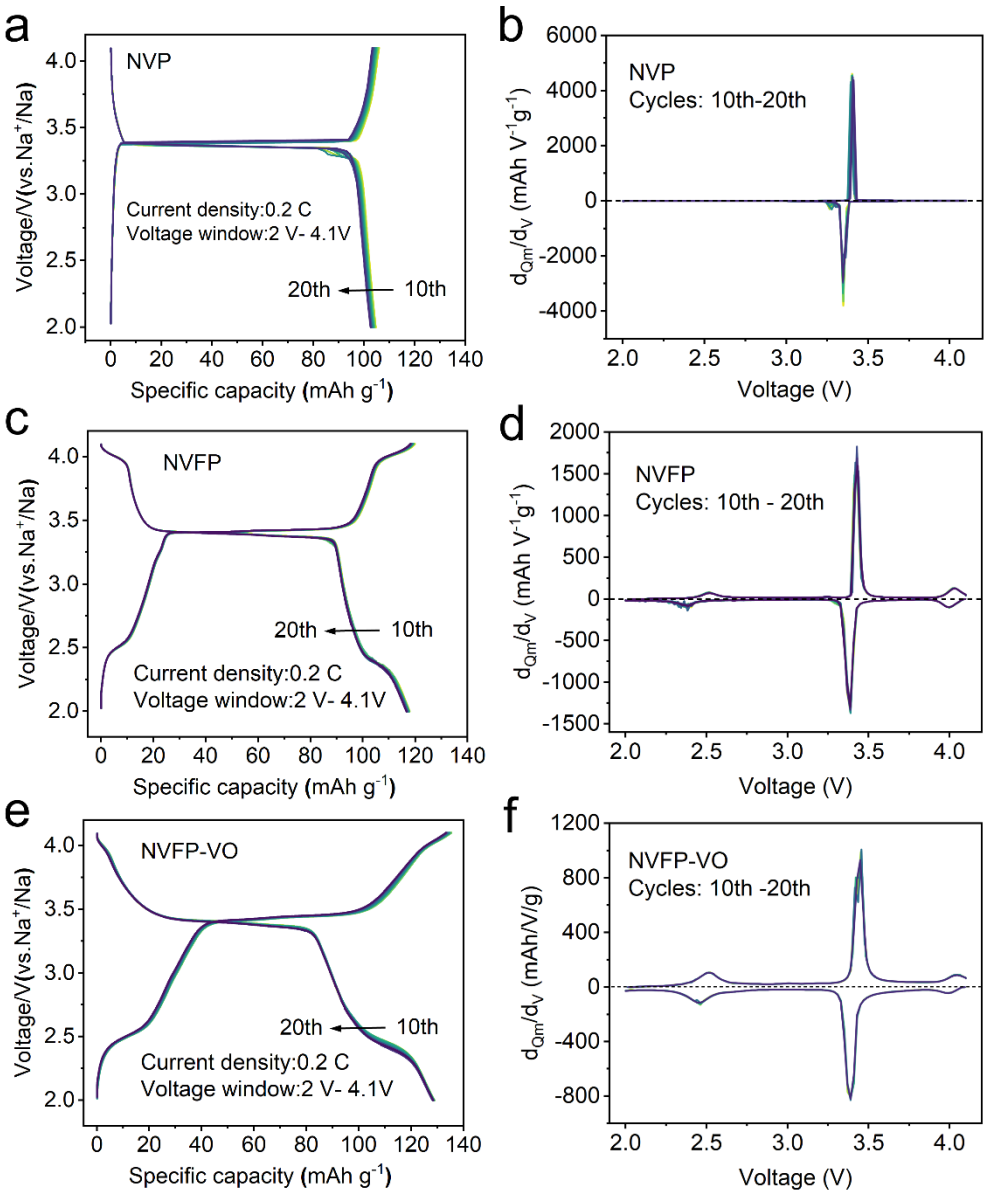

Figure S13. Charge-discharge and dQ_m/dV curves of **a-b** NVP, **c-d** NVFP, and **e-f** NVFP-VO.

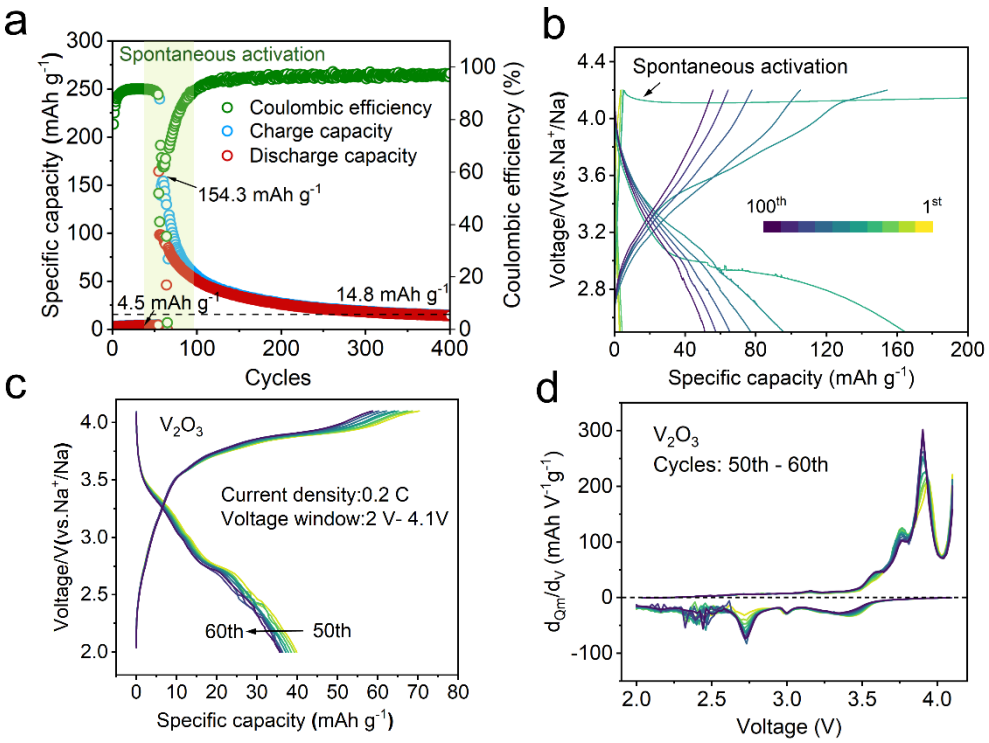

Figure S14. a Cycle performance, **b-c** charge-discharge curves and **d** dQ_m/dV curves of spontaneous activation V_2O_3.

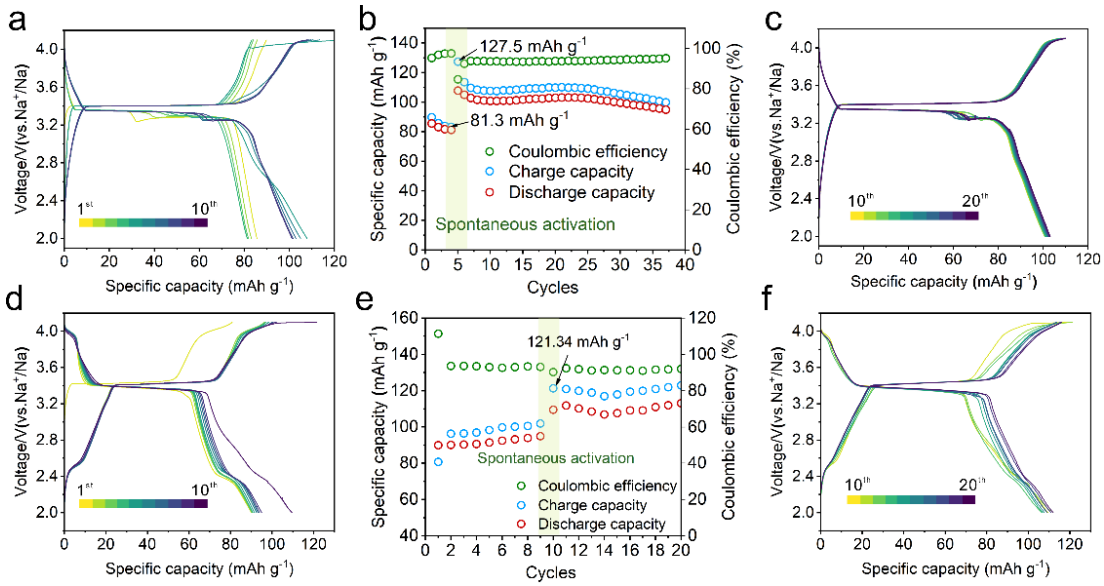

Figure S15. Charge-discharge curves of physically mixed NVP-V_2O_3 **a** before spontaneous activation, **b** cycle performance, **c** after spontaneous activation. Charge-discharge curves of physically mixed NVFP-V_2O_3 **d** before spontaneous activation, **e** cycle performance, **f** after spontaneous activation. (Current density: 0.2 C)

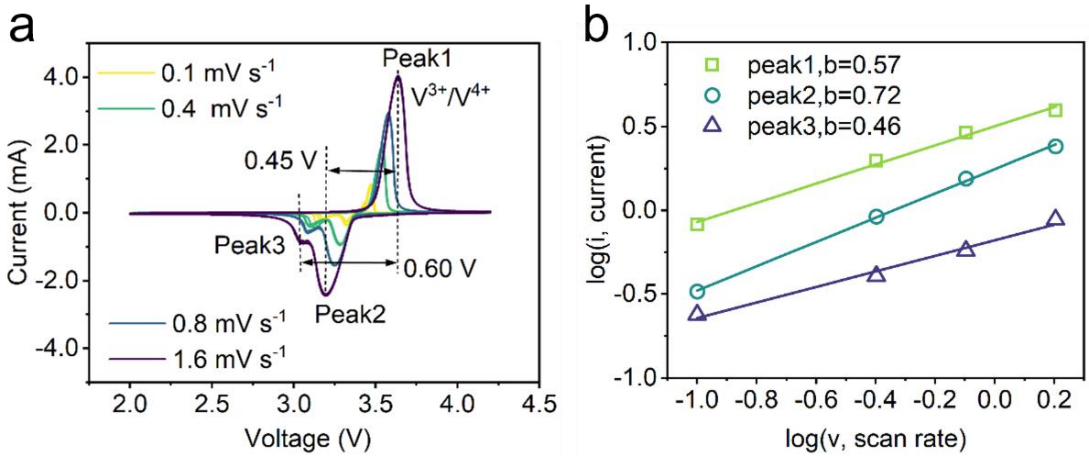

Figure S16. Calculation of the capacitance contribution. **a** CV curves of NVP electrode at various scan rates. **b** The log (v) versus log (i) plots for the different peaks in the CV curves, where i is the peak current and v is the scan rate.

For a redox reaction limited by semi-infinite diffusion, the peak current i varies as $v^{0.5}$; for a capacitive process, it varies as v. This relation is expressed as formula (1), with the value of b providing insight regarding the charge storage mechanism. Thus, the contribution of the capacitance can be calculated according to the following equations:

$$i = a\,v^{b} \tag{1}$$

$$log\,i = b \times log\,v + log\,a \tag{2}$$

where i is the peak current of the CV curves, v is the scan rate, and a and b are the fitting parameters. If the b-value approaches or is above 1, the electrochemical reaction system is mainly controlled via capacitance, while if the b-value approaches or is near 0.5, the insertion/de-insertion process for Na^+ ions will be the dominant behaviour.

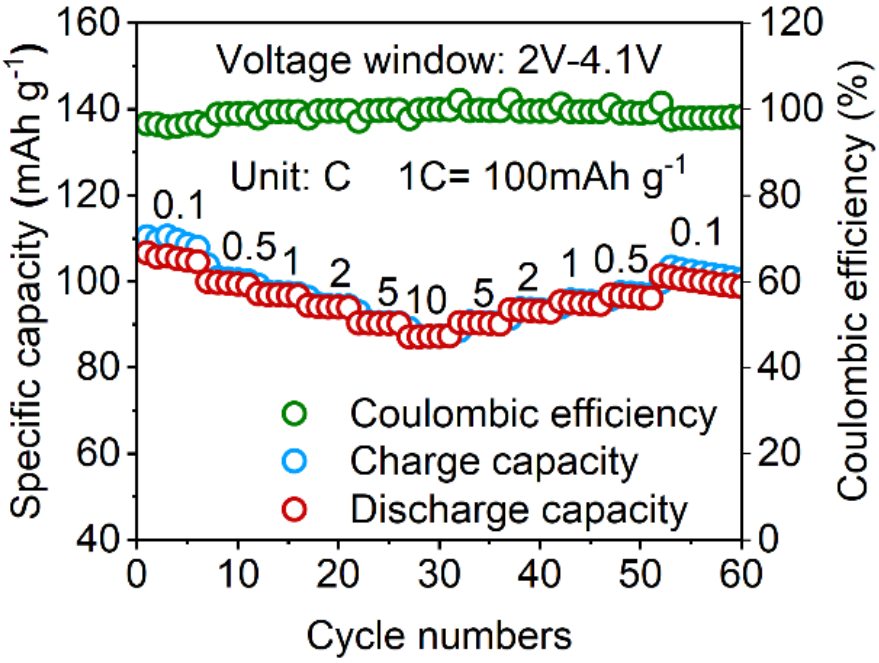

Figure S17. Rate performances of NVP cathode.

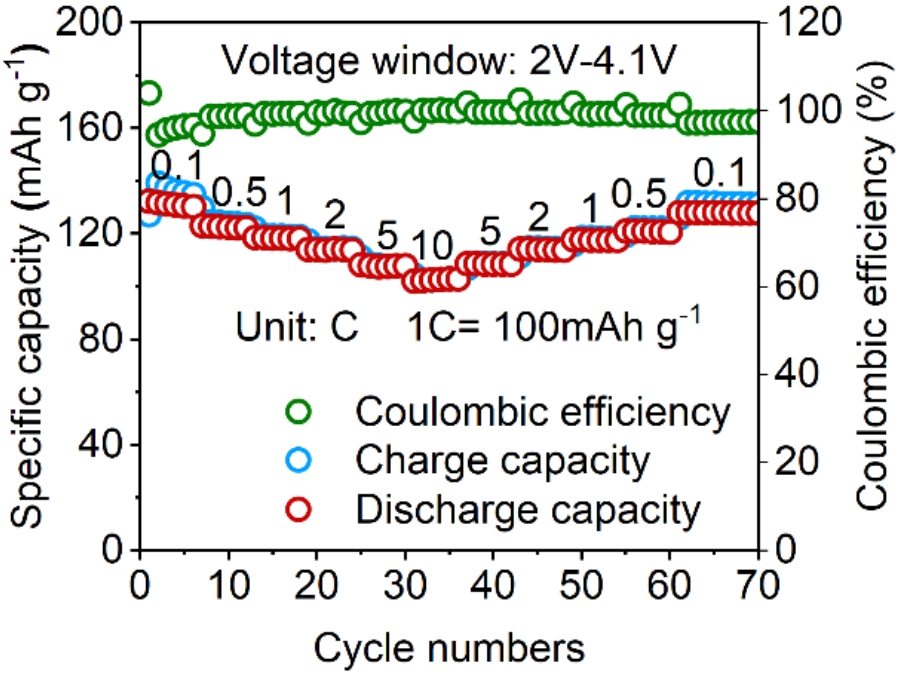

Figure S18. Rate performances of NVFP cathode.

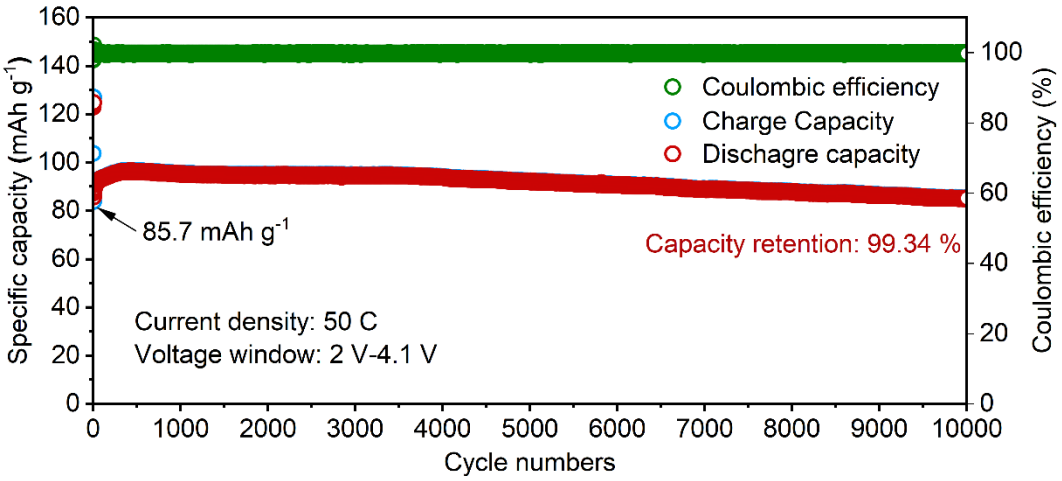

Figure S19. Cycling performance of NVFP-VO at 50 C.

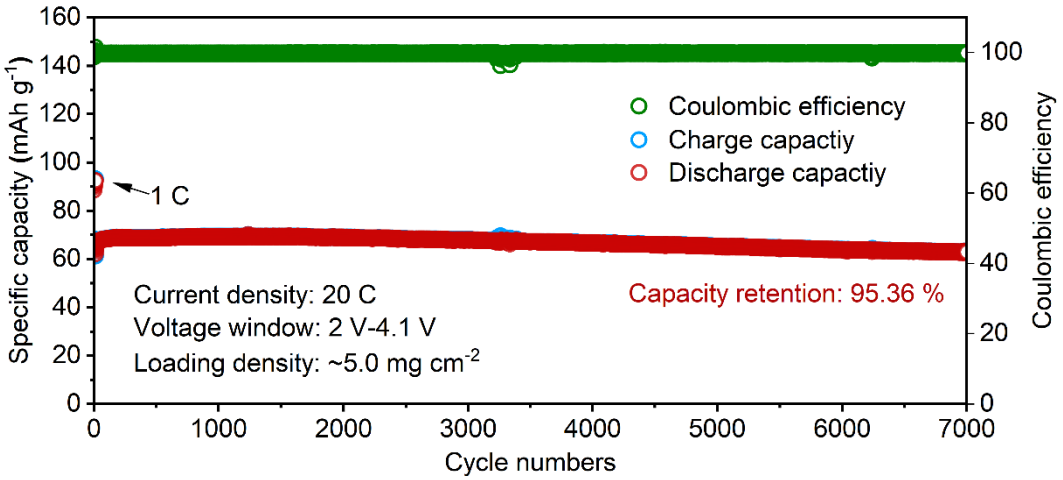

Figure S20. Long-term cycling performance of NVFP-VO for higher loading mass (~5.0 mg cm^{-2}) at 20 C.

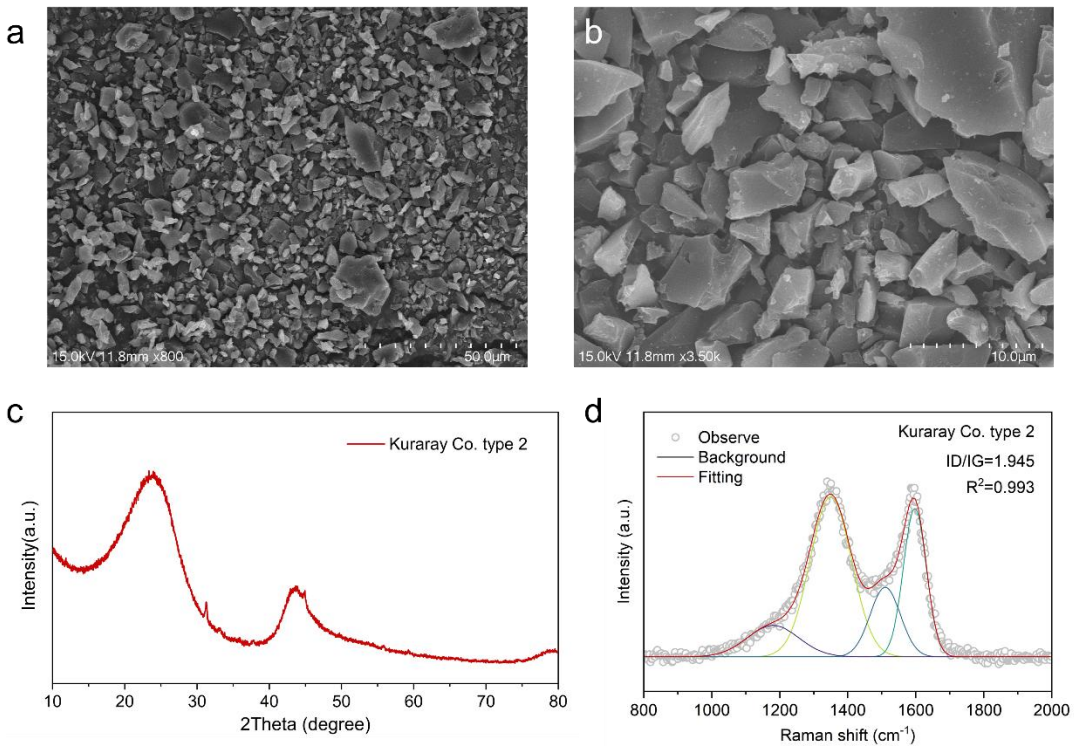

Figure S21. The characteristics of the commercial hard carbon anode material. SEM images of **a** commercial hard carbon, and **b** corresponding magnified image. **c** XRD result, **d** Raman spectrum with divided four bands, i.e., D4-, D1-, D3-, and G-bands (from small to large Raman shift respectively). R^2 is coefficient of determination.

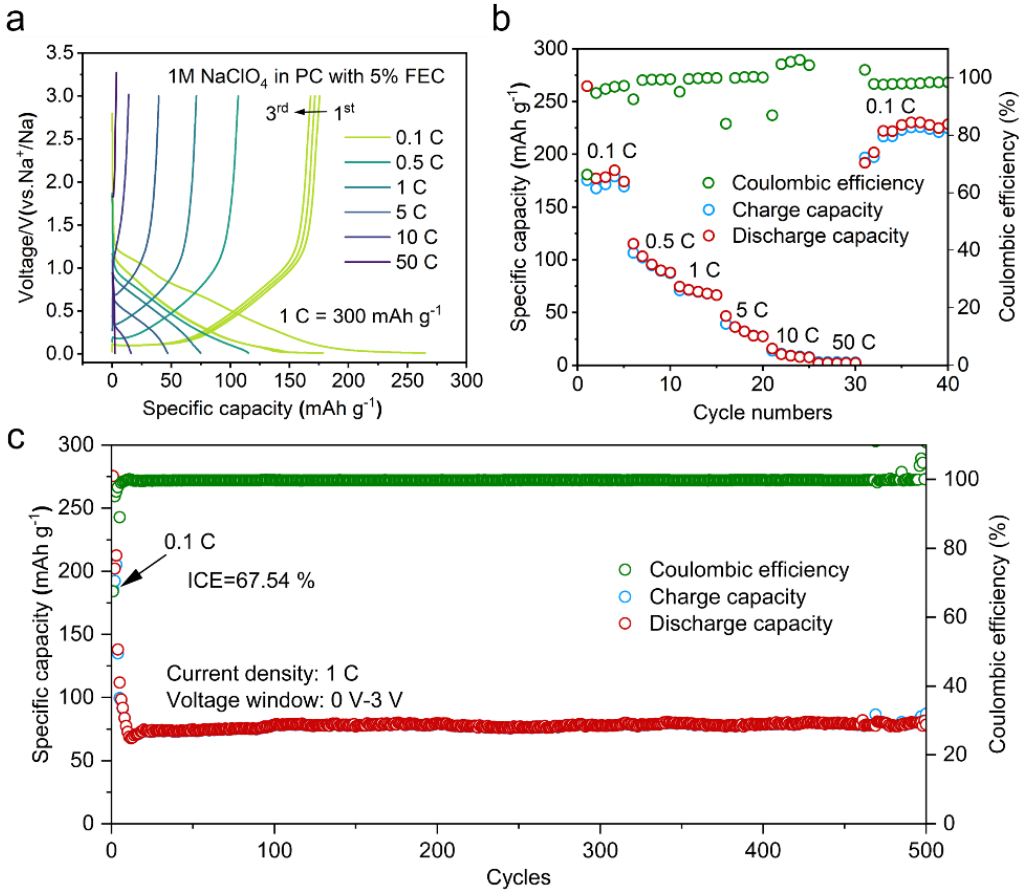

Figure S22. The Na storage performance of commercial hard carbon anode. **a** Charge-discharge curves (with the first three cycles), **b** cycle performance at different rates, and **c** long cycle performance using 1M $NaClO_4$ in PC with 5 vol% FEC as electrolyte.

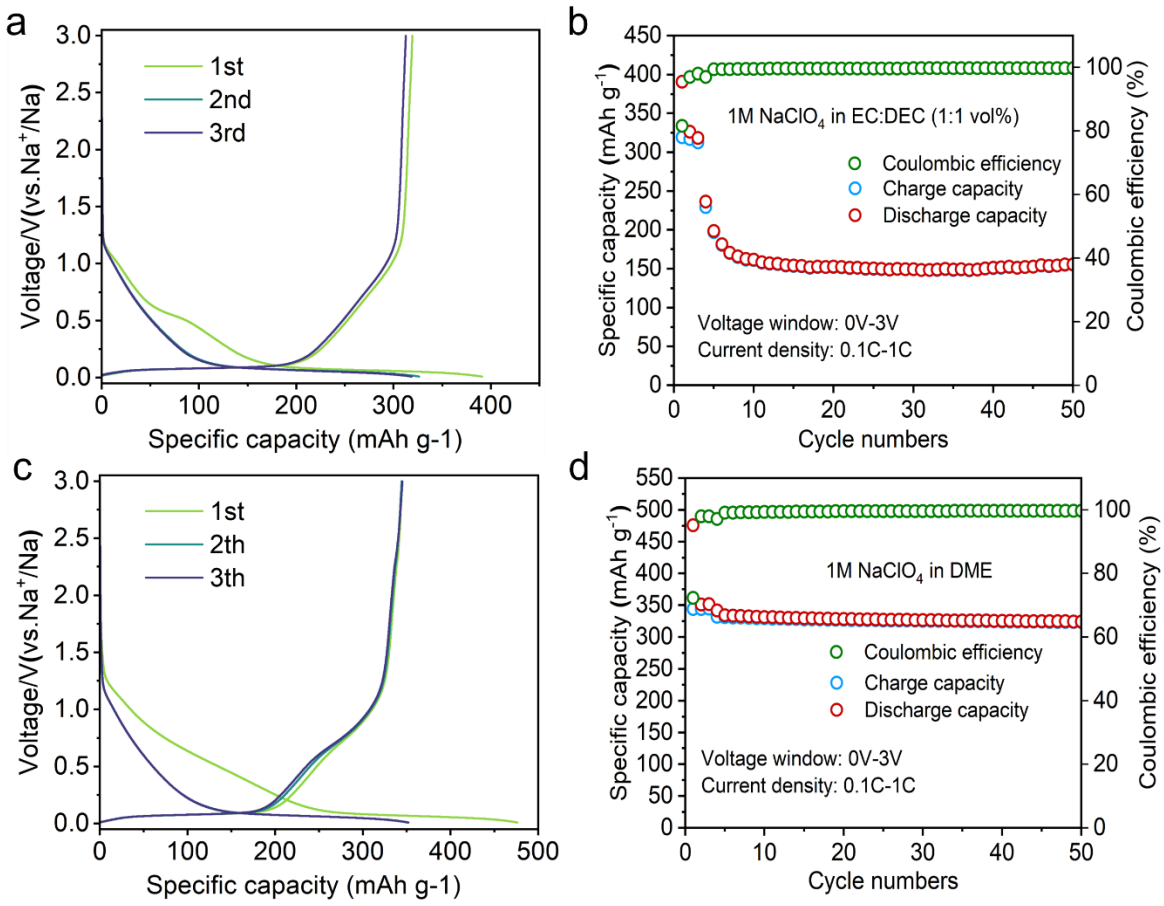

Figure S23. The Na storage performance of hard carbon anode. **a** Charge–discharge curves, **b** cycle performance using 1M $NaClO_4$ in EC:DEC (1:1 vol%) as electrolyte. **c** Charge–discharge profiles, and **d** cycle performance using 1M $NaClO_4$ in DME as electrolyte.

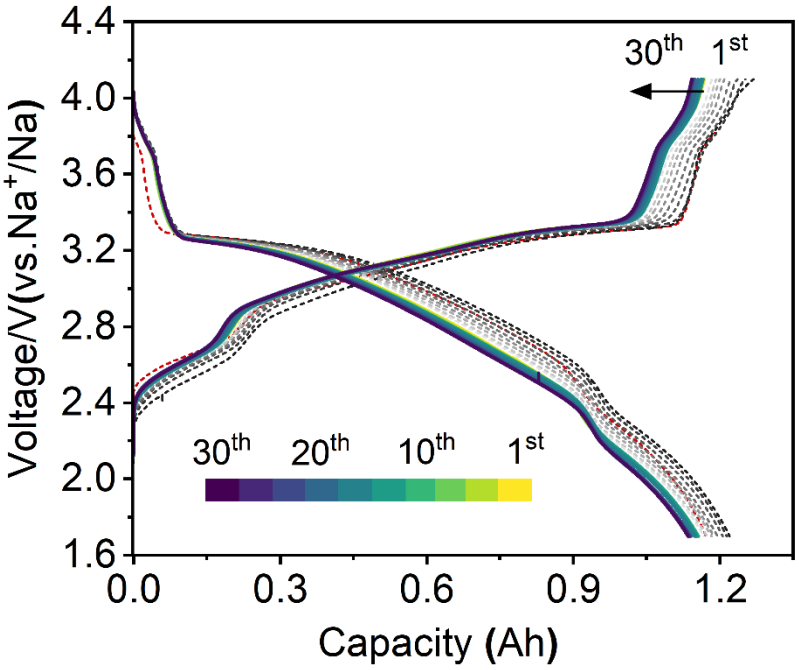

Figure S24. Pouch cell charge–discharge curves at 0.2 C (the gray dashed line is the curve of the aging process).

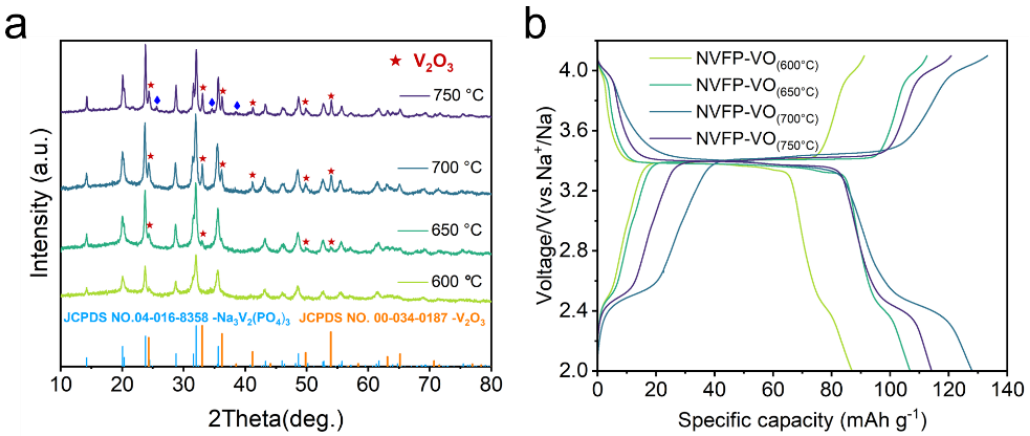

Figure S25. a XRD spectra and **b** charge-discharge curves of synthesized the precursor at different calcination temperatures.

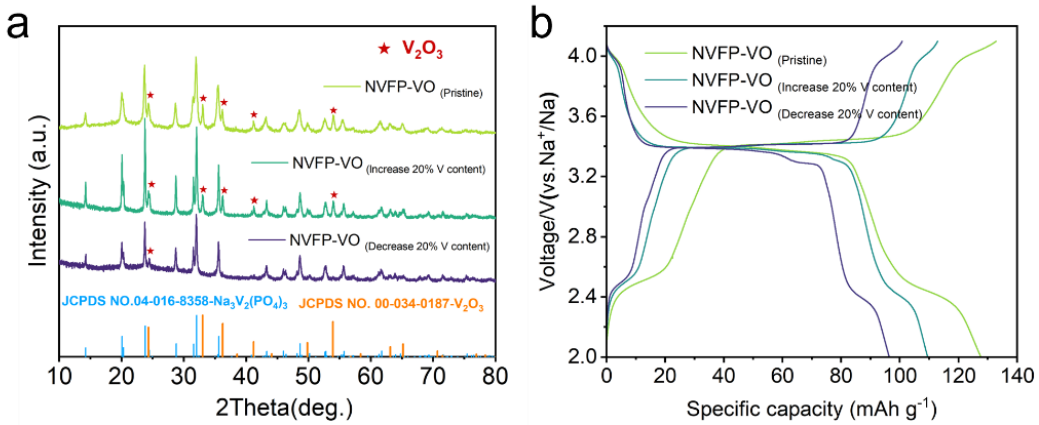

Figure S26. a XRD spectra and **b** charge-discharge curves of synthesized the precursor with different varying vanadium content.

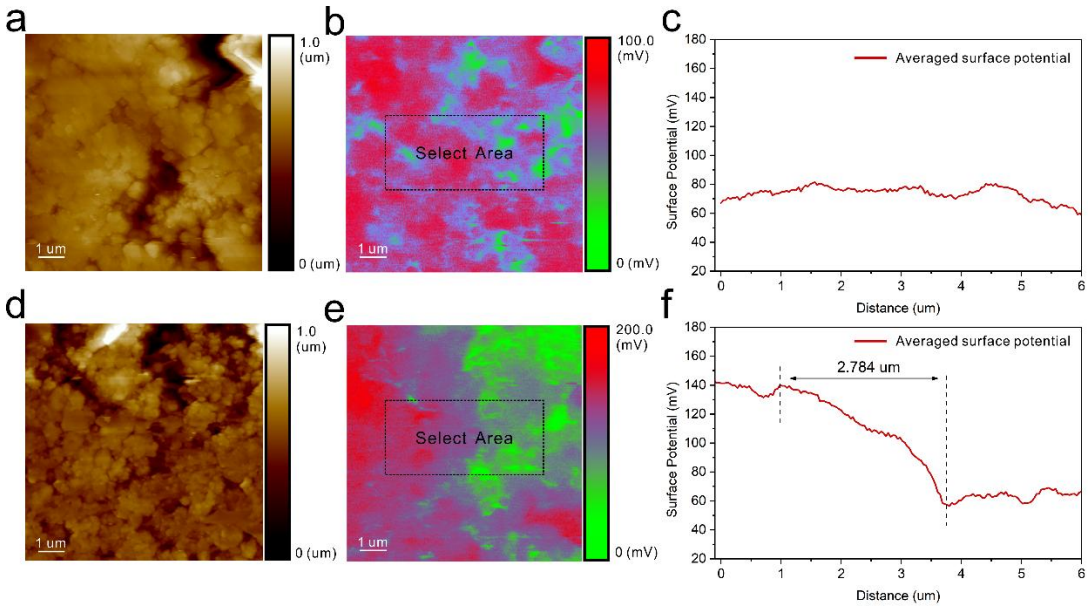

Figure S27. Kelvin probe force microscope (KPFM) analysis. Topographical images of **a** NVFP and **d** NVFP-VO samples. High spatial resolution surface potential distributions of **b** NVFP and **e** NVFP-VO samples. Locally averaged surface potential spectra derived from selected areas in (b) and (e), corresponding to **c** NVFP and **f** NVFP-VO samples, respectively.

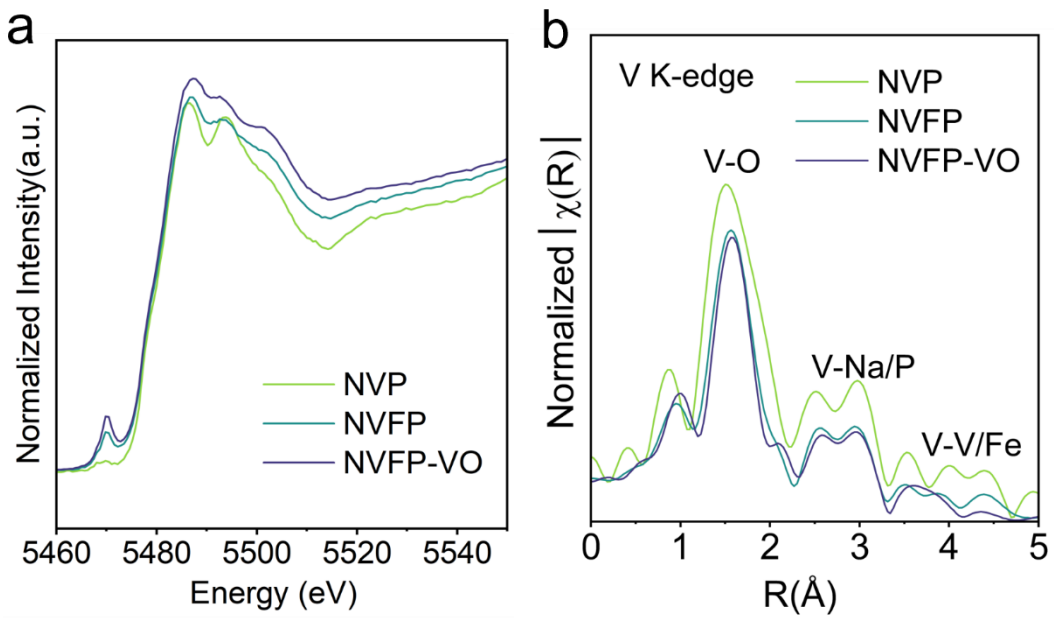

Figure S28. Ex situ XANES spectra of V K-edge of NVP, NVFP and NVFP-VO and corresponding Normalized ex situ EXAFS spectra.

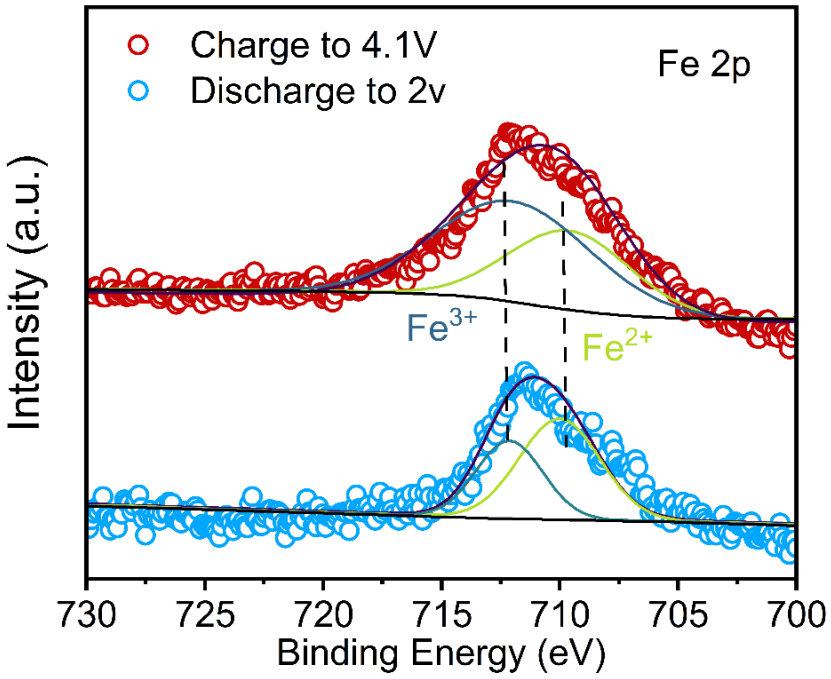

Figure S29. Ex situ high-resolution Fe 2p spectra of NVFP-VO at different SOC.

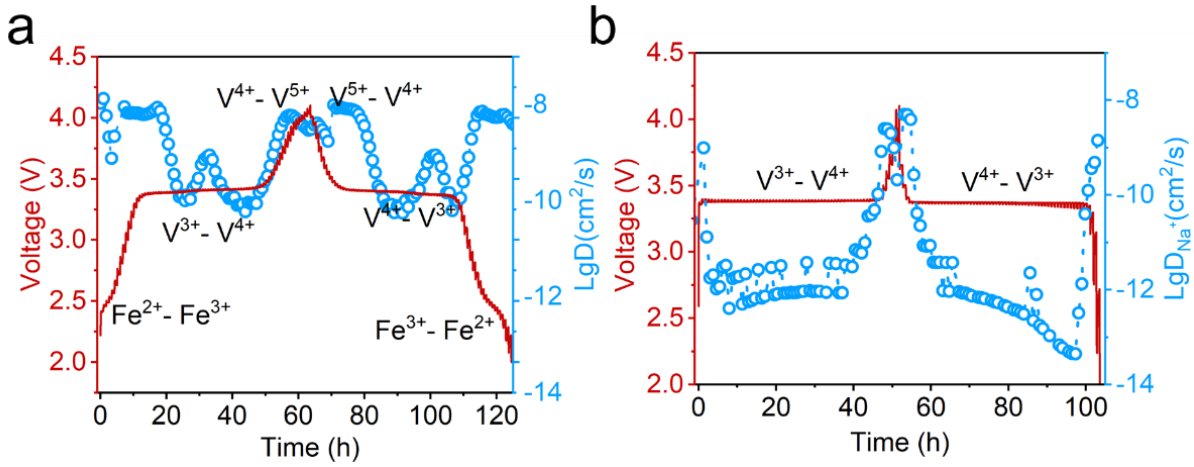

Figure S30. GITT experiment for **a** NVFP-VO and **b** NVP cathodes after 10 cycles to let the electrolyte/electrode reach its equilibrium state. (current density: 20 mA g^{-1}, 0.2 C).

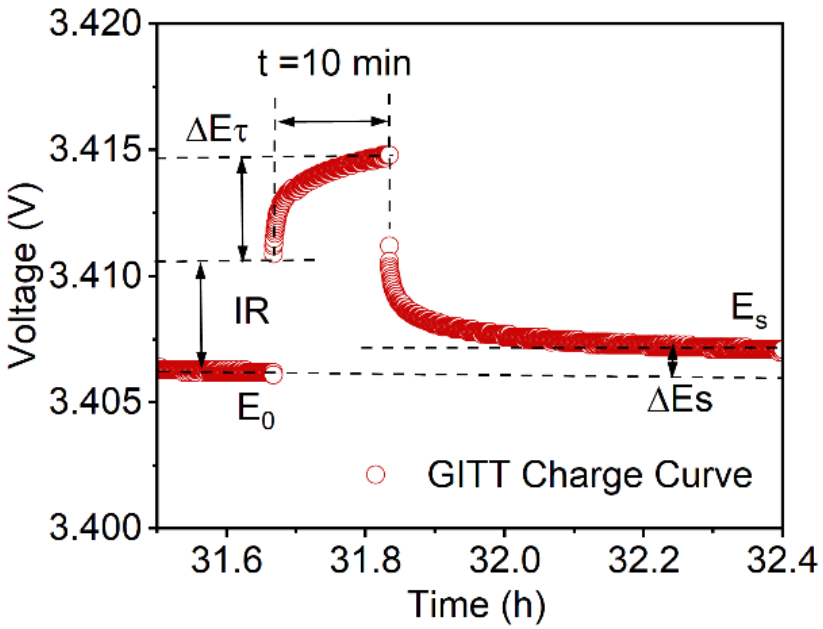

Figure S31. GITT experiment, showing a single pulse/rest step at around 3.4 V for the NVFP-VO electrode (current density: 20 mA g^{-1}, 0.2 C), annotated with key figures for calculating sodium diffusivity.

The Galvanostatic Intermittent Titration Technique (GITT) was used to analyze the reaction and diffusion kinetics at 20 mA g^{-1} specific current, 10 min charge/discharge time, and 40 min relaxor time. In the whole process of charge and discharge, the program is repeatedly applied to the battery. The diffusion process of sodium is anticipated to follow Fick's second law of diffusion. By simplifying a series of parameters, for sufficient rest time ($\tau \ll L^2/D_{Na^+}$), the diffusion coefficient of Na^+ (D_{Na+}, cm^{-2} s^{-1}) can be calculated based on the following formula:

$$D_{Na+} = \frac{4L}{\pi\tau}\left(\frac{\Delta E_s}{\Delta E_\tau}\right)^2$$

Where L is the thickness of the coated material on the carbon coating Al foil (200 μm), τ represents the duration of the current pulse (10 min) and π is considered to be 3.14159, ΔE_S is the difference in voltage at the end of consecutive rest steps (E_s-E_0), and $\Delta E\tau$ is the voltage change (V) during the constant current pulse.

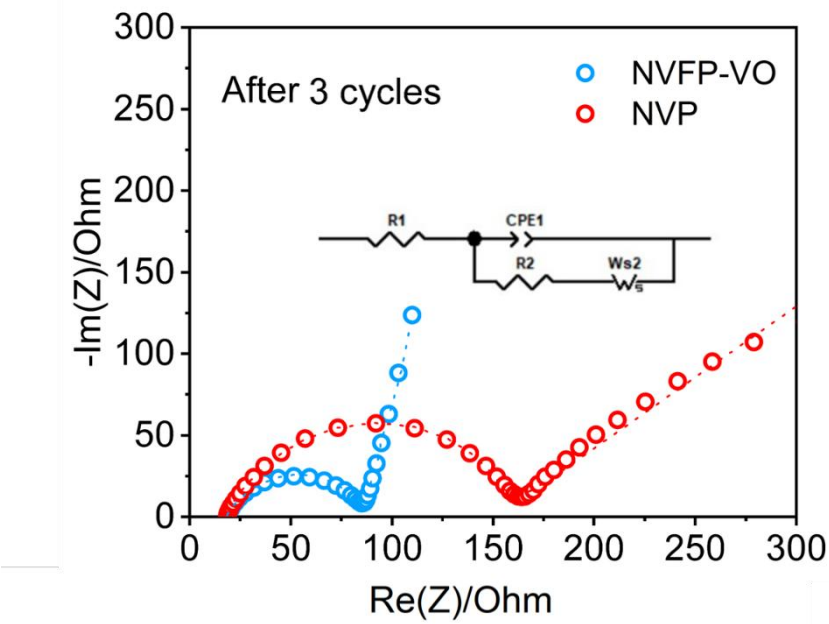

Figure S32. EIS experiment for the NVP and NVFP-VO electrodes after 3 cycles.

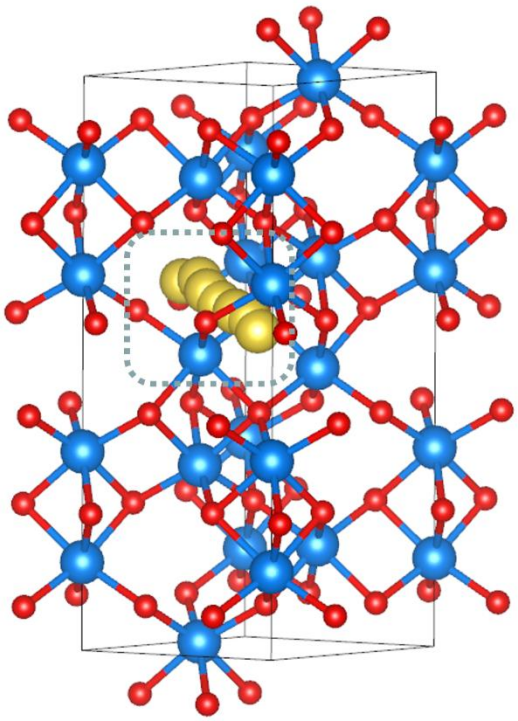

Figure S33. Schematic diagram of the Na^+ migration trajectory in V_2O_3.

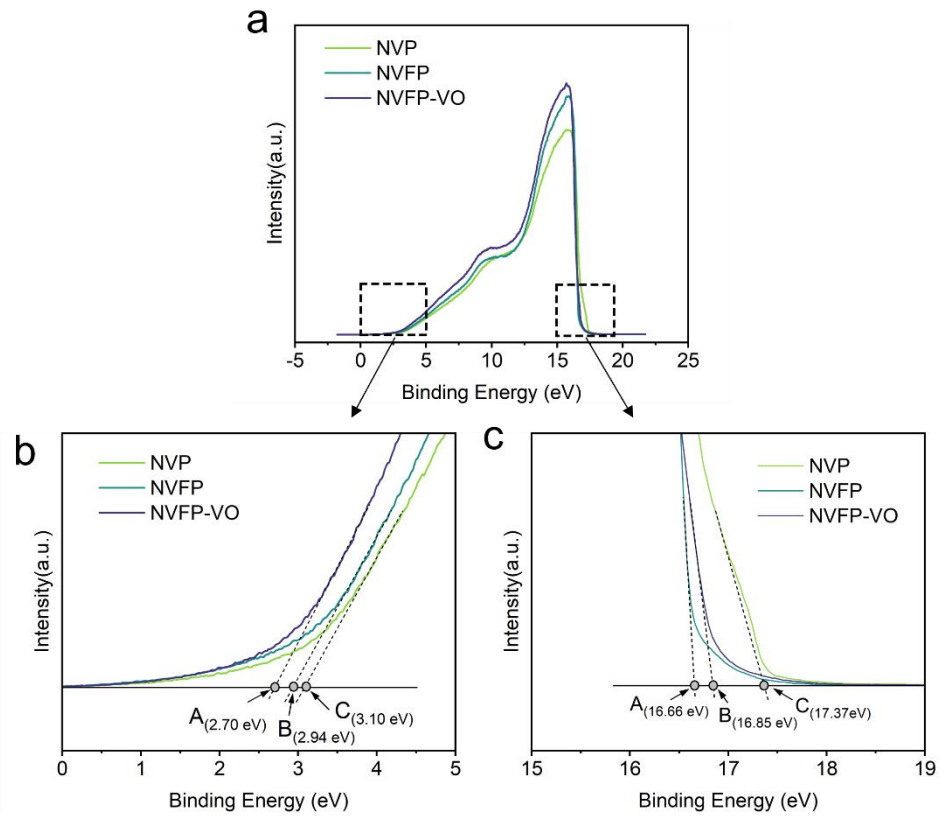

Figure S34. Ultraviolet photoelectron spectroscopy (UPS) analysis of NVFP and NVP. **a** Full spectrum, **b** 0-6 eV localized amplification spectrum, and **c** 15-19 eV localized amplification spectrum.

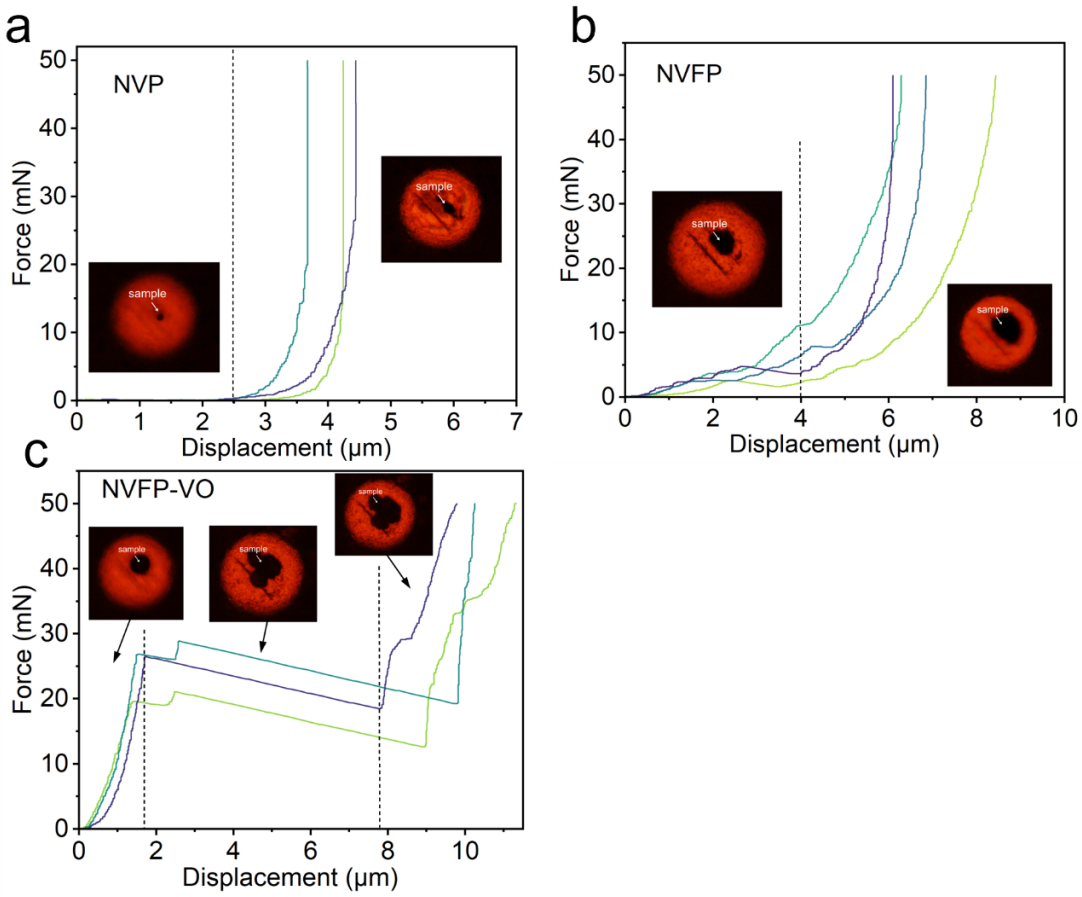

Figure S35. Single particle crush test force-displacement curves of **a** NVP, **b** NVFP, and **c** NVFP-VO.

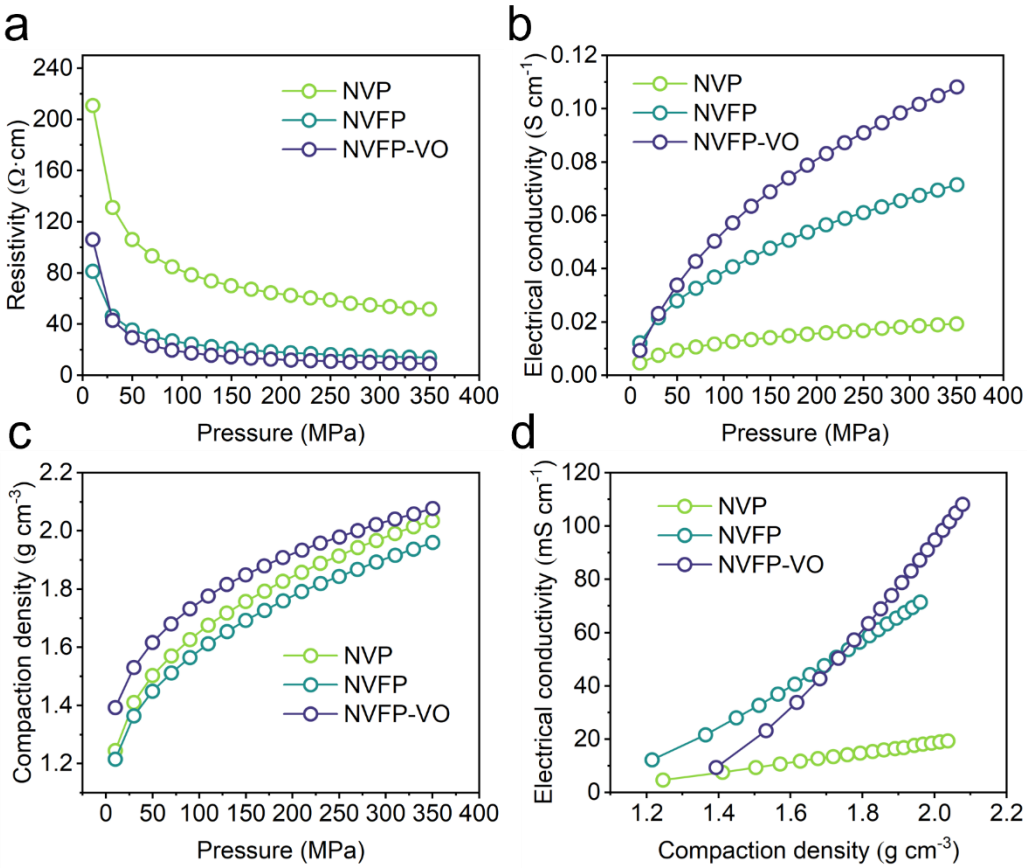

Figure S36. a The relationship between pressure and resistivity, **d** pressure and conductivity, **c** pressure and compaction density, **d** compaction density and conductivity of NVP, NVFP, and NVFP-VO samples.

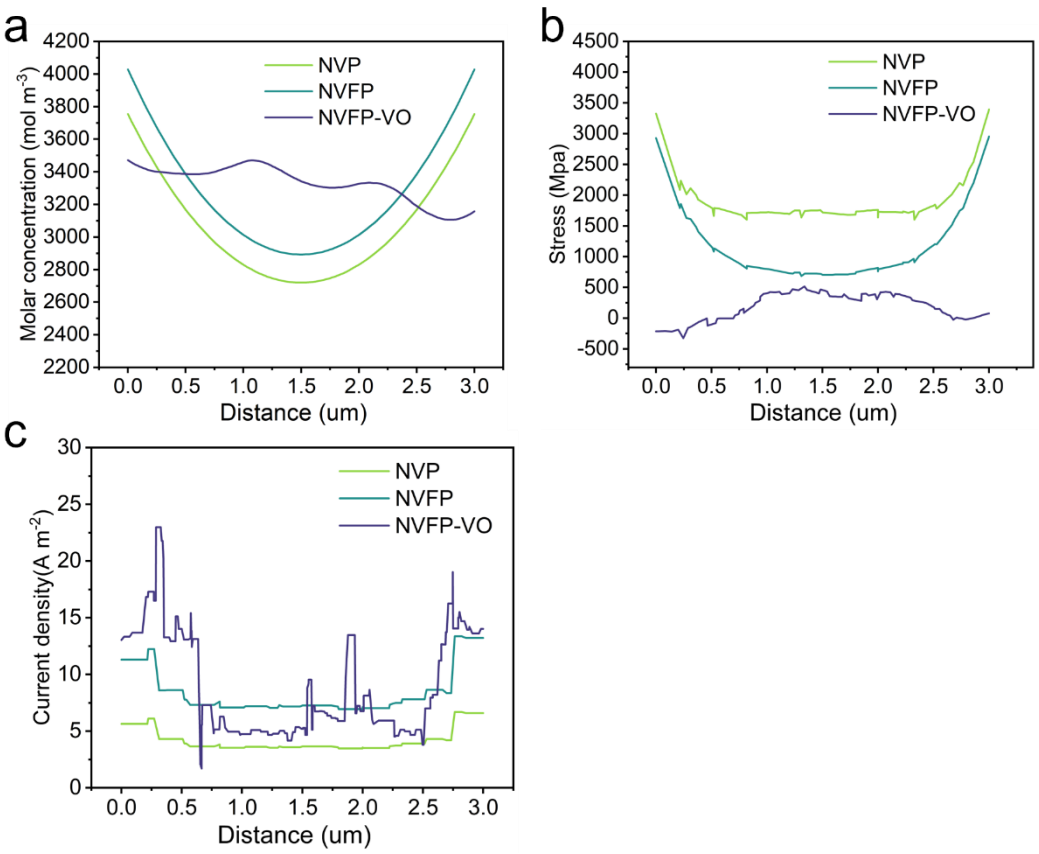

Figure S37. a Ions concentration distribution and distance from surface curves, **b** stress/strain distribution and distance from surface curves, and **c** current density and distance from surface curves of NVP, NVFP, and NVFP-VO samples.

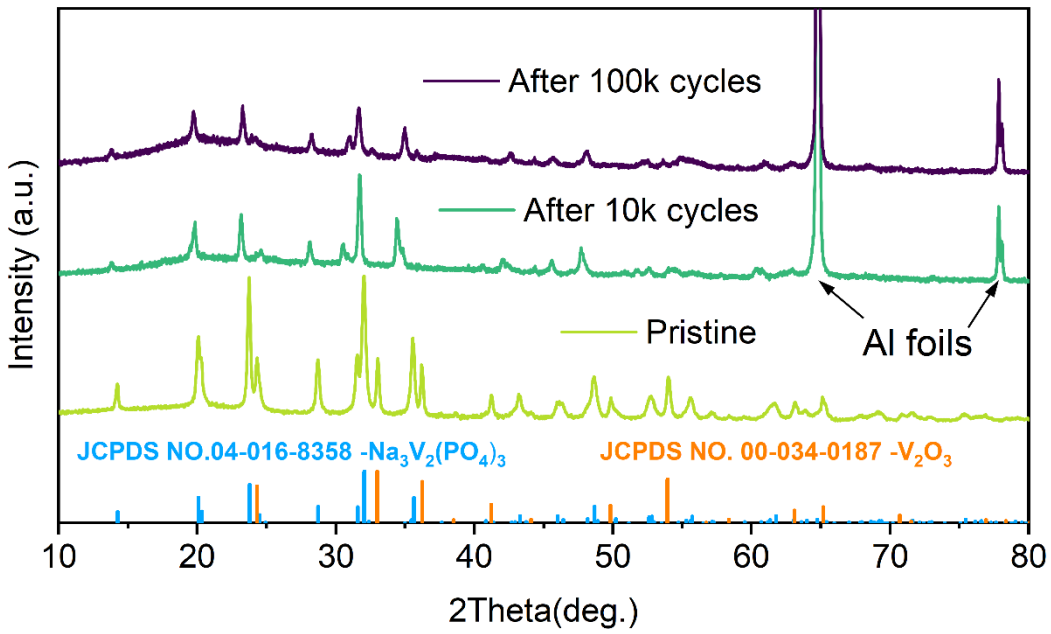

Figure S38. XRD spectra of pristine NVFP-VO material and cycled electrodes after different cycles.

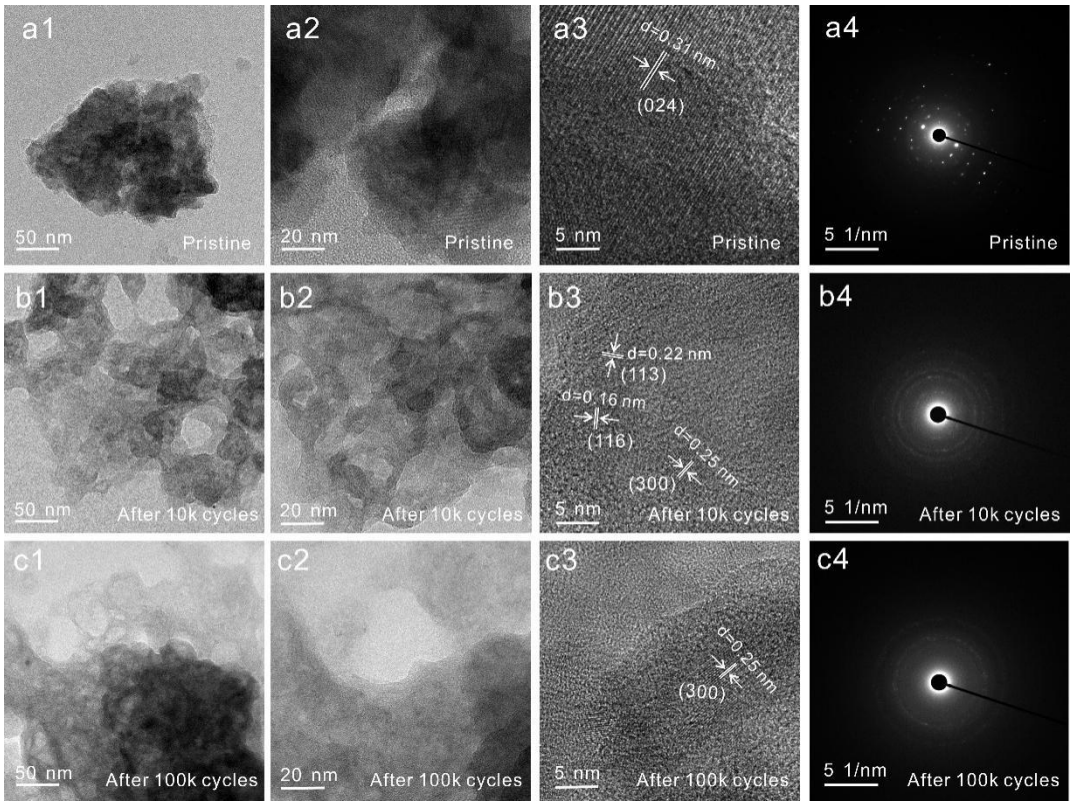

Figure S39. TEM images of pristine NVFP-VO material and cycled electrodes. TEM and HRTEM images of NVFP-VO electrode **a1-a3** pristine, **b1-b3** after 10,000 cycles and **c1-c3** after 100,000 cycles. **a4, b4, c4** present the corresponding SAED patterns of these electrodes.

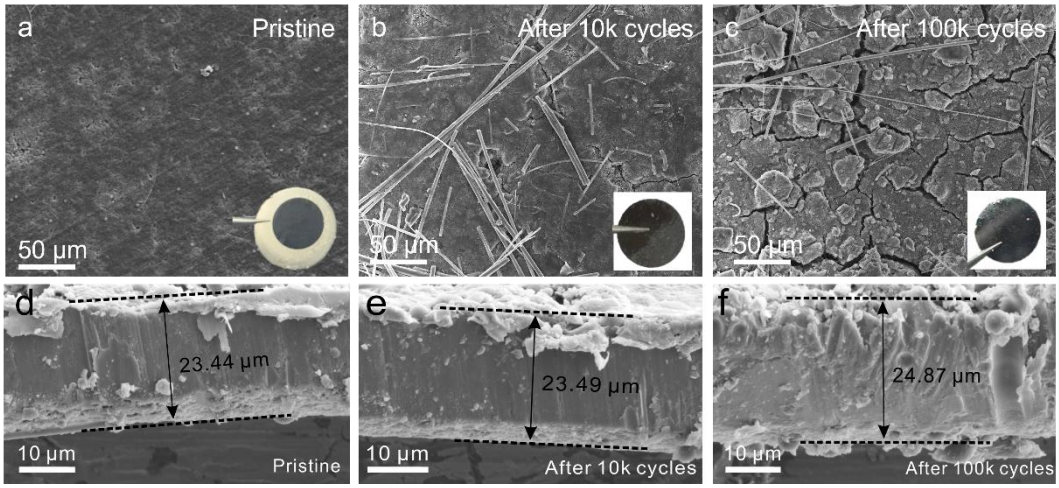

Figure S40. SEM images of pristine NVFP-VO electrode and cycled electrodes. NVFP-VO electrode **a** pristine, **b** after 10,000 cycles and **c** after 100,000 cycles. The insets in (a-c) are optic images of electrode after disassembly and the filiform streaks are glass fiber separators. SEM cross-section images of NVFP-VO **d** pristine electrode and **e, f** corresponding cycled electrodes.

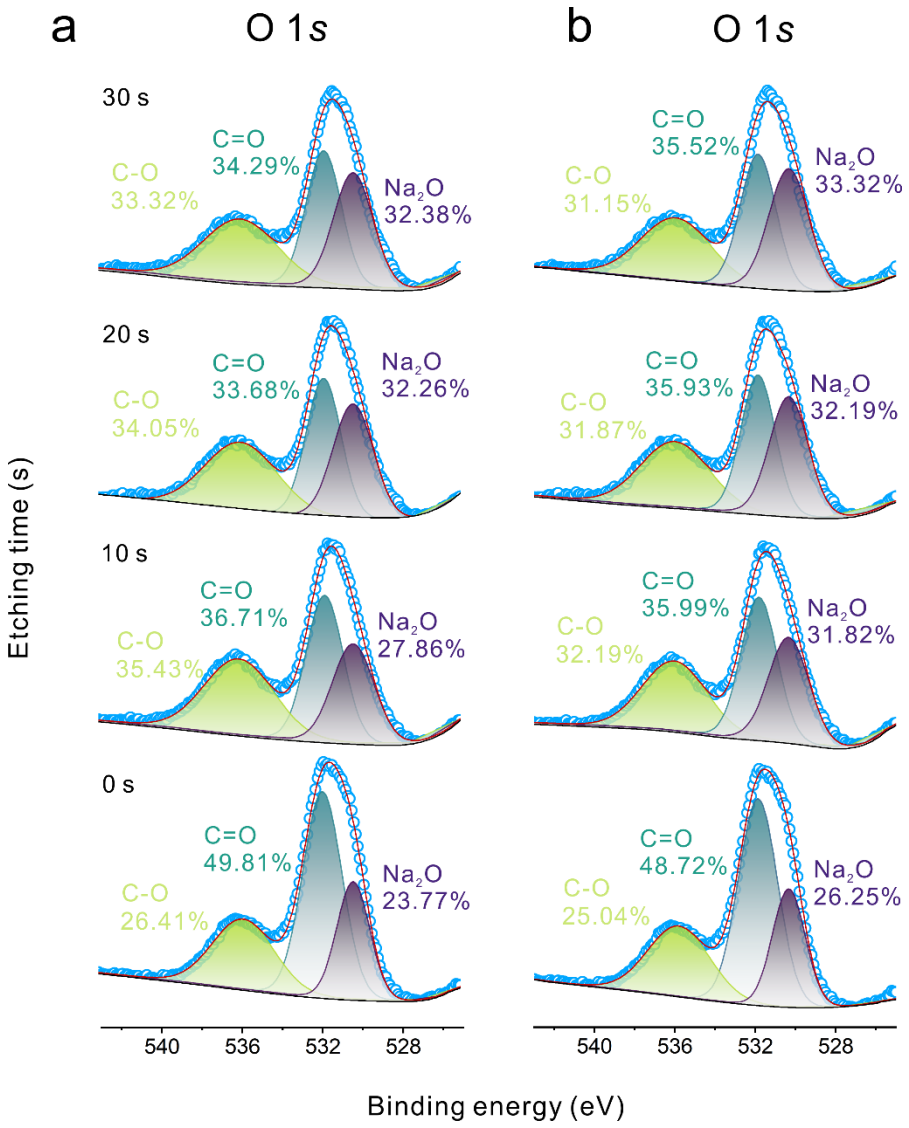

Figure S41. In-depth element distributions and high-resolution XPS spectra of O 1s.**a** NVP, **b** NVFP-VO.

Table S1. Detailed structural parameters of NVFP-VO from Rietveld refinement. Reliability factors of Rietveld refinement: R_{wp}=4.075%, R_{exp}=1.841%, R_p= 3.112%, Gof =2.213.

Phase 1: NVFP	Phase content: 90.693%±0.105 wt%		Space-group: *R-3c*		
Atom	**X**	**Y**	**Z**	**Occupancy**	**Cell parameters**
Na1	0.3333	0.6667	0.1667	1.0000	
Na2	0.6667	0.96037	0.0833	0.7622	a =8.72925±0.00051 Å
V1	0.3333	0.6667	0.01932	0.7500	b=8.72925±0.00051 Å
Fe1	0.3333	0.6667	0.01932	0.2500	c =21.80701±0.00132 Å
P1	0.95493	0.3333	0.0833	1.0000	α=β=90°
O1	0.14218	0.49794	0.07648	1.0000	γ=120°
O2	0.54775	0.84409	0.97413	1.0000	
Phase 2: V_2O_3	Phase content: 9.307%±0.105 wt%		Space-group: *R-3c*		
Atom	**X**	**Y**	**Z**	**Occupancy**	**Cell parameters**
V1	0.0000	0.0000	0.34634	1.0000	a = 4.95846±0.00031 Å b=4.95846±0.00031 Å c =13.97805±0.00104 Å
O1	0.3122	0.0000	0.25	1.0000	α=β=90° γ=120°

Table S2. The elemental ratio of the as-prepared samples determined by the ICP-OES measurements. Samples were prepared for ICP-OES by digesting 20-30 mg of samples in concentrated hydrochloric acid, then diluting in Milli-Q-purified H_2O until estimated concentrations were in a suitable range. All tests are replicated 3 times. Estimated relative uncertainties are less 10 %.

Samples	Refined crystal formula	Analyte concentrations (μg/mL)				Molar Ratios		
		Na	V	Fe	P	Na:P	V:P	Fe:P
NVP	$Na_{3.09}V_{1.97}(PO_4)_3$	3.918	5.538	/	5.111	1.033	0.658	/
NVFP	$Na_{3.51}V_{1.27}Fe_{0.48}(PO_4)_3$	5.271	4.234	1.763	6.086	1.166	0.422	0.1604
NVFP-VO	$Na_{3.45}V_{2.36}Fe_{0.49}P_3O_x$	4.653	7.040	1.607	5.451	1.145	0.785	0.1634
NVFP-VO (+20%)	$Na_{3.42}V_{2.83}Fe_{0.42}P_3O_x$	3.893	7.134	1.185	4.595	1.140	0.943	0.1427
NVFP-VO (-20%)	$Na_{3.36}V_{1.84}Fe_{0.43}P_3O_x$	4.725	5.784	1.476	5.723	1.112	0.614	0.1429

Table S3. The electrochemical performance comparison with other typical phosphate cathodes reported (in chronological order). [6–14]

Year	Cathode	Cycling stability	Rate perfermance	Voltage window	Reference
2019	$Na_{3.5}V_{1.5}Mn_{0.5}(PO_4)_3$	96.8 mA h g^{-1} at 500th cycle at 5 C (90.7% retention) 87.8 mA h g^{-1} at 4000th cycle at 20 C (87.1 % retention)	108.6 mAh g^{-1} at 1C 108.3 mAh g^{-1} at 2 C 108.3 mAh g^{-1} at 5 C 107.0 mAh g^{-1} at 10 C 104.5 mAh g^{-1} at 20 C 100.1 mAh g^{-1} at 40 C 92.7 mAh g^{-1} at 60 C	2.5-4.1 V	Energy Storage Materials 23 (2019) 25–34
2019	$Na_{3.75}V_{1.25}Mn_{0.75}(PO_4)_3$	89.44 mA h g^{-1} at 100th cycle at 1 C (86% retention)	100 mAh g^{-1} at 1 C 95 mAh g^{-1} at 2 C 89 mAh g^{-1} at 5 C	2.75-3.8 V	Adv. Energy Mater. 2019, 1902918
2020	$Na_4MnCr(PO_4)_3$	47.7 mA h g^{-1} at 600th cycle at 5 C (86.5 % retention)	114.1 mAh g^{-1} at 0.1 C 106.2 mAh g^{-1} at 0.2 C 99.5 mAh g^{-1} at 0.5 C 86.3 mAh g^{-1} at 1 C 73.5 mAh g^{-1} at 2 C 60.5 mAh g^{-1} at 5 C 43.2 mAh g^{-1} at 10 C 26.6 mAh g^{-1} at 15 C	1.4-4.3 V	Adv. Energy Mater. 2020, 1903968
2021	$Na_{3.41}\square_{0.59}FeV(PO_4)_3$	108 mA h g^{-1} at 300th cycle at 5 C (99.4 % retention) 93 mA h g^{-1} at 700th cycle at 10 C (94.7 % retention)	119 mAh g^{-1} at 0.5C 117 mAh g^{-1} at 2C 111 mAh g^{-1} at 5C 104 mAh g^{-1} at 10C	2-3.8 V	Energy Storage Materials 35 (2021) 192–202

		80 mA h g^{-1} at 400th cycle at 20 C (98.4 % retention)			
2021	$Na_4VMn_{0.5}Fe_{0.5}(PO_4)_3$	103.5 mA h g^{-1} at 500th cycle at 5 C (99.3 % retention) 76.8 mA h g^{-1} at 3000th cycle at 20 C (94.2 % retention)	120 mAh g^{-1} at 0.5 C 113.6 mAh g^{-1} at 1 C 109.2 mAh g^{-1} at 2 C 106.0 mAh g^{-1} at 5 C 103.1 mAh g^{-1} at 10 C 95.5 mAh g^{-1} at 20 C	Rate 2.0-4.0 V Cycling 2.0-3.8 V	Adv. Energy Mater. 2021, 11, 2100729
2022	$Na_3Cr_{0.5}V_{1.5}(PO_4)_3$@VC/C-G	141.5 mA h g^{-1} at 100th cycle at 0.2 C (80.4 % retention) 97.7 mA h g^{-1} at 500th cycle at 5 C (80.4 % retention) ~64 mA h g^{-1} at 1000th cycle at 20 C (53.3 % retention)	176.0 mAh g^{-1} at 0.2 C 160.4 mAh g^{-1} at 0.5 C 152.8 mAh g^{-1} at 1 C 144.9 mAh g^{-1} at 3 C 141.2 mAh g^{-1} at 5 C 130.5 mAh g^{-1} at 10 C 113.4 mAh g^{-1} at 20 C 101.9 mAh g^{-1} at 30 C 94.8 mAh g^{-1} at 50 C	1.5-4.1 V	Adv. Energy Mater. 2022, 2201065
2022	$Na_{3.4}V_{1.6}Fe_{0.4}(PO_4)_3$	98 mA h g^{-1} at 900th cycle at 5 C (94% retention) 97.6 mA h g^{-1} at 2000th cycle at 20 C (96% retention)	108.0 mA h g^{-1} at 0.5 C 106.7 mA h g^{-1} at 1 C 105.2 mA h g^{-1} at 2 C 103.9 mA h g^{-1} at 5 C 102.9 mA h g^{-1} at 10 C 101.7 mA h g^{-1} at 20 C	2.5-4.1 V	Adv. Energy Mater. 2022, 12, 2200966
2023	$Na_{3.5}V_{1.5}Fe_{0.5}(PO_4)_3$	105 mA h g^{-1} at 1000th cycle at 1 C (~99 % retention)	112 mA h g^{-1} at 0.5 C 105 mA h g^{-1} at 1 C 96 mA h g^{-1} at 5 C 68 mA h g^{-1} at 100 C	2-3.8 V	Adv. Mater. 2023, 35, 2304428

		96.0 mA h g^{-1} at 1000th cycle at 5 C (92 % retention) 78.7 mA h g^{-1} at 10,000th cycle at 100 C (84 % retention) 141 mA h g^{-1} at 280th cycle at 1 C (~99 % retention) 92.2 mA h g^{-1} at 500th cycle at 5 C (72 % retention) ~60 mA h g^{-1} at 10,000th cycle at 100 C (66.8 % retention)	148.2 mA h g^{-1} at 0.5 C 142.4 mA h g^{-1} at 1 C 128.1 mA h g^{-1} at 5 C 73.5 mA h g^{-1} at 100 C	1.7-4.3 V	
2024	$Na_3V_2(PO_4)_3$/NVDs	~98 mA h g^{-1} at 400th cycle at 5 C (95.4 % retention) ~51.1 mA h g^{-1} at 20,000th cycle at 200 C (98.4 % retention)	113.9 mA h g^{-1} at 1 C 113.0 mA h g^{-1} at 2 C 110.9 mA h g^{-1} at 5 C 108.9 mA h g^{-1} at 10 C 104.1 mA h g^{-1} at 20 C 86.9 mA h g^{-1} at 50 C 78.5 mA h g^{-1} at 70 C 69.6 mA h g^{-1} at 90 C 66.7 mA h g^{-1} at 100 C	2.0-4.0 V	Adv. Energy Mater. 2024, 2400595
2024	$Na_{4.5}Fe_{3.5}(PO_4)_2.5(P_2O_7)$	~108 mA h g^{-1} at 3000th cycle at 5 C (96 % retention) ~93 mA h g^{-1} at 11,000th cycle at 20 C	130 mA h g^{-1} at 0.1 C ~125 mA h g^{-1} at 0.2 C ~120 mA h g^{-1} at 0.5 C ~115 mA h g^{-1} at 2 C ~110 mA h g^{-1} at 5 C	2-4.2 V	J. Am. Chem. Soc. 2024, 146, 9819-9827

		(88 % retention)	~108 mA h g^{-1} at 10 C 103 mA h g^{-1} at 20 C		
This work	NVFP-VO	~85 mA h g^{-1} at 10,000th cycle at 50 C (99 % retention) ~43 mA h g^{-1} at **100,000th** cycle at **100 C** (72 % retention)	132.2 mA h g^{-1} at 0.1 C 126.9 mA h g^{-1} at 0.5 C 124.3 mA h g^{-1} at 1 C 121.1 mA h g^{-1} at 2 C 115.4 mA h g^{-1} at 5 C 109.9 mA h g^{-1} at 10 C 109.5 mA h g^{-1} at 20 C 96.3 mA h g^{-1} at 50 C 81.7 mA h g^{-1} at 100 C	2-4.1 V	This work

Table S4. The Parameters for the 153.4 W h kg^{-1} Na-ion pouch cell.

Parameter	Value for the NVFP-VO||HC pouch cell
Cathode mass loading (NVFP-VO:95 wt%)	~15.4 mg cm^{-2}
Anode mass loading (HC:95 wt%)	~18.5 mg cm^{-2}
Area capacity (single face)	~1.85 mA h cm^{-2}
Active area (five folds double face)	650 cm^2 (13.0×5.0 cm^2)
N/P ratio	1.2
Electrolyte	1M $NaClO_4$ in PC with 5 vol% FEC, 6.0 g Ah^{-1}
Current collector	Al foil:10um
Separator	Clegard 2325
Capacity	1.2 Ah
Average output voltage	2.9 V
Energy density	153.4 W h kg^{-1}

Table S5. The elemental concentration of electrodes after cycling were determined by the ICP-OES measurements. All disassembled electrode samples were process by immersion in PC solvent for 24 h and then diluted until the estimated concentrations were in the appropriate range. All tests are replicated 3 times. Estimated relative uncertainties are less 5 %. The values in parentheses are normalized based on the P element.

Samples	Analyte concentrations (mg/L)			
	Na	V	Fe	P
NVFP (after cycles)	1.062125 (59.22)	0.0218 (1.22)	0.0147 (0.82)	0.01794 (1)
NVFP-VO (after cycles)	0.816528 (53.95)	0.0096 (0.63)	0.0061 (0.40)	0.01514 (1)

Table S6. The Fitting parameters of EIS spectra.

Electrodes	R_1	R_2
NVP	18.526	167.768
NVFP-VO	18.502	87.027

Reference

1 G. Kresse and J. Furthmüller, *Phys. Rev. B.*, 1996, **54**, 11169–11186.

2 G. Kresse and J. Furthmüller, *Comp. Mater. Sci.*, 1996, **6**, 15–50.

3 J. P. Perdew, K. Burke and M. Ernzerhof, *Phys. Rev. Lett.*, 1996, **77**, 3865–3868.

4 G. Kresse and D. Joubert, *Phys. Rev. B.*, 1999, **59**, 1758–1775.

5 P. E. Blöchl, *Phys. Rev. B.*, 1994, **50**, 17953–17979.

6 M. Hadouchi, N. Yaqoob, P. Kaghazchi, M. Tang, J. Liu, P. Sang, Y. Fu, Y. Huang and J. Ma, *Energy Storage Mater.*, 2021, **35**, 192–202.

7 R. Rajagopalan, B. Chen, Z. Zhang, X.-L. Wu, Y. Du, Y. Huang, B. Li, Y. Zong, J. Wang, G.-H. Nam, M. Sindoro, S. X. Dou, H. K. Liu and H. Zhang, *Adv. Mater.*, 2017, **29**, 1605694.

8 S. Ghosh, N. Barman, M. Mazumder, S. K. Pati, G. Rousse and P. Senguttuvan, *Adv. Energy Mater.*, 2020, **10**, 1902918.

9 J. Zhang, Y. Liu, X. Zhao, L. He, H. Liu, Y. Song, S. Sun, Q. Li, X. Xing and J. Chen, *Adv. Mater.*, 2020, **32**, 1906348.

10 J. Wang, Y. Wang, D. Seo, T. Shi, S. Chen, Y. Tian, H. Kim and G. Ceder, *Adv. Energy Mater.*, 2020, **10**, 1903968.

11 W. Zhang, Y. Wu, Z. Xu, H. Li, M. Xu, J. Li, Y. Dai, W. Zong, R. Chen, L. He, Z. Zhang, D. J. L. Brett, G. He, Y. Lai and I. P. Parkin, *Adv. Energy Mater.,* 2022, **12**, 2201065.

12 W. Zhou, L. Xue, X. Lü, H. Gao, Y. Li, S. Xin, G. Fu, Z. Cui, Y. Zhu and J.

B. Goodenough, *Nano Lett.*, 2016, **16**, 7836–7841.

13 J. Zhang, X. Zhao, Y. Song, Q. Li, Y. Liu, J. Chen and X. Xing, *Energy Storage Mater.*, 2019, **23**, 25–34.

14 C. Xu, J. Zhao, E. Wang, X. Liu, X. Shen, X. Rong, Q. Zheng, G. Ren, N. Zhang, X. Liu, X. Guo, C. Yang, H. Liu, B. Zhong and Y.-S. Hu, *Adv. Energy Mater.*, 2021, **11**, 2100729.